Coordination Chemistry Reviews 255 (2011) 2068–2093

Contents lists available at ScienceDirect

Coordination Chemistry Reviews

journal homepage: www.elsevier.com/locate/ccr

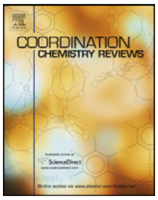

Review

Thermo-, piezo-, photo- and chemo-switchable spin crossover iron(II)-metallocyanate based coordination polymers

M. Carmen Muñoz[a], José A. Real[b,*]

[a] Departamento de Física Aplicada, Universitat Politècnica de València, Camino de Vera s/n, E-46022, València, Spain
[b] Instituto de Ciencia Molecular (ICMol), Universidad de Valencia, C/Catedrático José Beltrán Martínez, 2, 46980 Paterna, Valencia, Spain

Contents

ARTICLE INFO

Article history:
Received 10 December 2010
Accepted 10 February 2011
Available online 22 February 2011

Keywords:
Coordination polymers
Spin crossover
Iron(II) compounds
Metallocyanate anions

ABSTRACT

The design of coordination polymers (CPs) with switch and memory functions is an important subject of current interest in the search for new advanced materials with potential applications. Implementation of CPs with electronically labile iron(II) building blocks able to undergo cooperative spin crossover (SCO) behavior is a singular approach to this end. This review provides an up to date survey of a new generation of iron(II)-metallocyanate based spin crossover coordination polymers (SCO-CPs) developed during the last decade. These new solids feature structural diversity, supramolecular isomerism, interpenetrating frameworks, structure flexibility, reversible solid-state chemical reactions, metallophilic interactions, porosity, physi- and chemisorption, or processability at nanoscale level, in addition to inherent SCO properties.

1. Introduction

It is well known that the iron(II) ion in octahedral surroundings can adopt two different electronic configurations, $t_{2g}^4e_g^2$ and $t_{2g}^6e_g^0$, that depend on the ligand field strength. The former electronic con-

---

* Corresponding author.
E-mail addresses: mcmunoz@fis.upv.es (M.C. Muñoz), jose.a.real@uv.es (J.A. Real).

0010-8545/$ – see front matter © 2011 Elsevier B.V. All rights reserved.
doi:10.1016/j.ccr.2011.02.004

figuration corresponds to the paramagnetic high-spin (HS) state while the latter corresponds to the diamagnetic low-spin (LS) state. Most iron(II) compounds belong to one of these families. However, when the energy gap between the two states is close to the thermal energy a new family of compounds appears called spin crossover (SCO). These compounds can adopt both spin states and change from one state to the other state in a reversible, controllable and detectable way by the action of external stimuli like temperature, pressure, light, and even an analyte [1].

Given the antibonding nature of the e_g orbitals their population–depopulation provokes drastic structural changes in the coordination sphere of iron(II). In the solid state these changes are transmitted cooperatively from one active site to another through elastic interactions. When these interactions are weak the cooperativity is poor and the spin change is continuous. On the contrary, when the interactions are strong the cooperativity is strong and the magnetic, optical, dielectric and structural properties change drastically. In special cases these drastic changes are accompanied by hysteretic behavior, which confers to the material bistable character. Bistability is an important property associated with memory and sensory functions, which could ultimately be useful for the elaboration of molecule-based devices [2].

Two synthetic approaches have been employed to achieve cooperativity. The so-called supramolecular approach seeks to maximize intermolecular interactions between SCO centers. Hydrogen bonding and π–π interactions are the most important sources of cooperativity in discrete SCO systems [3]. In the polymeric approach, the intermolecular links between SCO active centers are substituted partially or totally for more reliable coordinative bonds, thereby generating spin crossover coordination polymers (SCO-CPs). When the bridging ligands are rigid enough, cooperative spin transitions can be observed. Two paradigmatic examples of the polymeric approach are the one-dimensional (1D) compound $[Fe(Htrz)_2(trz)](BF_4)$ (Htrz is 1,2,4-triazole, trz is the triazolate anion) [4] and the two-dimensional (2D) compound $[Fe(btrz)_2(NCS)_2]\cdot H_2O$ shown in Fig. 1 [5]. Both compounds have been important sources of inspiration for the synthesis of new 1-3D SCO-CPs since they undergo strong cooperative spin transitions (ST) accompanied by remarkable hysteretic behavior. It is worth noting that the use of bismonodentate ligands, L, like bpe (trans-1,2-bis(4-pyridyl)ethylene) [6] or azpy (4,4′-azopyridine) [7] instead of btr has afforded relevant SCO-CPs formulated $[Fe(L)_2(NCS)_2]\cdot n$solvent. The greater length of the organic bridges L with respect to btr usually favors interpenetration of identical 2D layers, thereby generating voids where the solvent molecules are installed (see Fig. 2). However, despite interesting structures and functions displayed by these and other related compounds, the lack of rigidity of the bridging ligand L usually makes the SCO poorly cooperative and incomplete. Furthermore, this strategy is essentially limited to the generation of 1- and 2-D SCO-CPs since the pseudo-halide coordinating anion is not an appropriate bridging ligand. These facts motivated the search for alternative synthetic paradigms and prompted the use of metallocyanate complexes as anionic bridges, which has opened important scenarios in the synthesis of new 1-3 D SCO-CPs.

The aim of this article is to survey the range of iron(II)-metallocyanate based coordination polymers that exhibit spin-transitions. This will provide a convenient guide to what materials

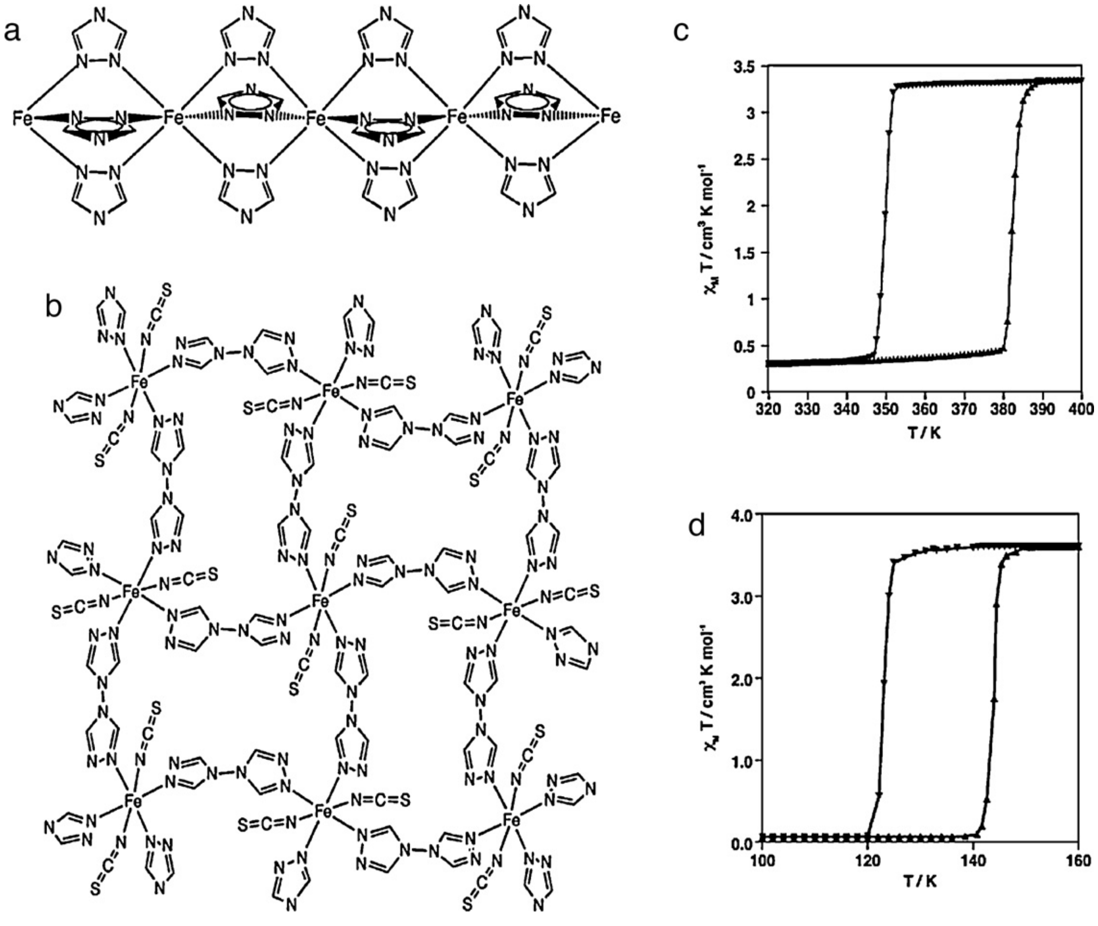

Fig. 1. Schematic view of the 1D system $[Fe(Htrz)_2(trz)](BF_4)$ (a), 2D system$[Fe(btr)_2(NCS)_2]$ (b) and their respective magnetic behaviors (c and d) (χ_M is the magnetic susceptibility and T is temperature).

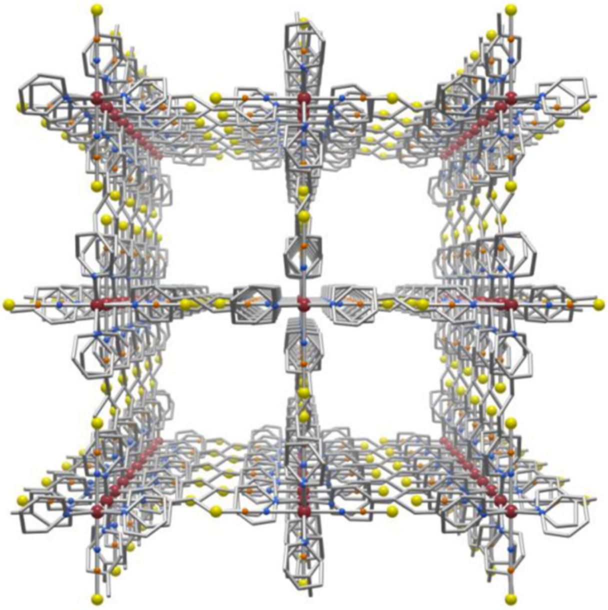

Fig. 2. Fragment of the 2D CP [Fe(bpe)$_2$(NCS)$_2$] showing the orthogonal interpenetration and generation of large square channels. Color code: Fe (red), S (yellow), N (blue), and C (grey).

have been made in the last decade, highlighting those that exhibit interesting spin-transitions and/or structural chemistry. The next four sections are organized according to the different types of metallocyanate ligands ([M^{I}(CN)$_2$]$^-$ (M^I = Cu, Ag, Au); [M^{II}(CN)$_4$]$^{2-}$ M^{II} = Ni, Pd, Pt; [M^{III}(CN)$_6$]$^{3-}$ (M^{III} = Cr) and [M^{IV}(CN)$_6$]$^{4-}$ (M^{IV} = Nb). In general, in these sections we shall describe first the essential structural features and subsequently the spin crossover properties. Two sections devoted to porous spin crossover coordination polymers and processability at nanoscale level will follow before some concluding remarks.

2. Dicyano-cuprate complexes

2.1. Structure

Self-assembly of Fe(II), [Cu(CN)$_2$]$^-$ and the organic ligands L = 3-cyanopyridine [8], 3-halogenpyridine (3Xpy, X = CN, F, Cl, Br, I) [9] or pyrimidine (pmd) [10] has afforded a series of CPs that exhibit a variety of one-(1D), two-(2D) and three-(3D) dimensional metal-organic frameworks. A common feature in this series is the expansion of the coordination sphere of Cu(I), in the linear [Cu(CN)$_2$]$^-$ species, to adopt distorted trigonal [CuL(CN)$_2$]$^-$ or tetrahedral [CuL$_2$(CN)$_2$]$^-$ geometries. The resulting CPs have the general formula {Fe(3Xpy)$_2$[Cu(3Xpy)$_n$(CN)$_2$]$_2$} abbreviated **Cu3Xpy**.

When X = CN, Cl, Br or I and n = 1, the solids crystallize in the triclinic *P*-1 space group with the crystal packing determined by stacking of infinite 1D linear chains. In these chains the Fe(II) ion, located at an inversion center, defines a pseudoctahedral [FeN$_6$] coordination site with two 3Xpy groups occupying the axial positions while four equatorial positions are occupied by N atoms of the *in situ* generated [Cu(3Xpy)(CN)$_2$]$^-$ bridges (Fig. 3 left). The bridging NC–Cu–CN moiety strongly deviates from 180° (**Cu3CNpy**: 117–120°; **Cu3Clpy** (α-polymorph): 125.8°; **Cu3Brpy**: 123.9°; **Cu3Ipy**: 126.2°). These angles predispose the formation of linear chains (Fig. 3 right). The chains assemble in well-defined layers. In **Cu3CNpy** the layers are sustained by short Cu···Cu metallophilic contacts, 2.6358 Å, smaller than the sum of the van der Waals radii (2.8 Å). In contrast, interdigitation of the 3Xpy groups characterizes the packing of the chains for the remaining members of this series, where no intermetallic interactions occur. Interestingly, a monoclinic P2$_1$/c form of the **Cu3Clpy** derivative has also been described. In this β-polymorph, deviation of the NC–Cu–CN angle from 180° is noticeably smaller than in the precedent cases (144.1–145.6° (LS) to ca 148° (HS)), thus facilitating the formation of a 3D four-connected network with the expanded structure of the prototypal open-framework CdSO$_4$ (Fig. 4). Both α- and β-polymorphs represent an example of architectural isomerism since they have the same chemical formula but different polymeric structures.

A different situation has been observed for **3FpyCu** formulated {Fe(3Fpy)$_2$[Cu(3Fpy)$_{1.5}$(CN)$_2$]$_2$}. It is made up of strongly corrugated 2D grids constituted by edge-sharing [Fe$_4$] squares whose edges are defined by distorted pseudo-trigonal [Cu(3Fpy)(CN)$_2$]$^-$ and pseudo-tetrahedral [Cu(3Fpy)$_2$(CN)$_2$]$^-$ anions (Fig. 5). This 2D arrangement seems to be the result of distinct NC–Cu–CN angles defined by the pseudo-trigonal (144.3°) pseudo-tetrahedral (130.7°) bridges.

In {Fe(pmd)$_2$[Cu(CN)$_2$]$_2$} (**Cupmd**) the copper(I) ion satisfies the tendency to expand its coordination number in a different way. The Fe(II) atoms lie at the inversion center of an elongated octahedron whose equatorial and axial positions are occupied by [Cu(CN)$_2$]$^-$ and pmd bridging groups, respectively. [Cu(CN)$_2$]$^-$ connects Fe(II) atoms while the pmd bridges pairs of Cu(I) and Fe(II) ions. The marked deviation from linearity of the NC–Cu–CN angle (C–Cu–C is ca 118.5°), due to coordination of the pmd, generates linear chains linked through the pmd ligand originating a 2D CP with the topol-

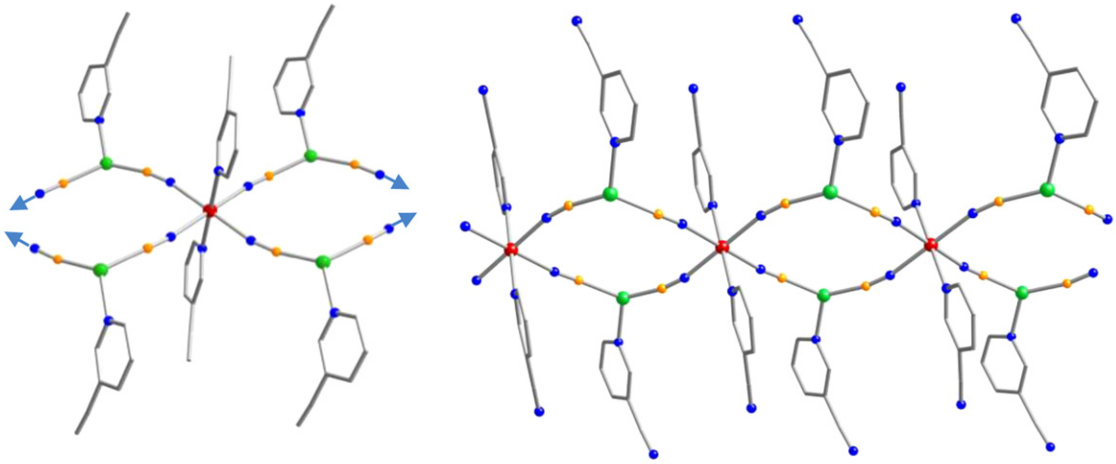

Fig. 3. Coordination surroundings of the Fe(II) and Cu(I) centers (left) and view of a fragment of chain (right). Color code: Fe (red), Cu (green), N (blue), and C (orange).

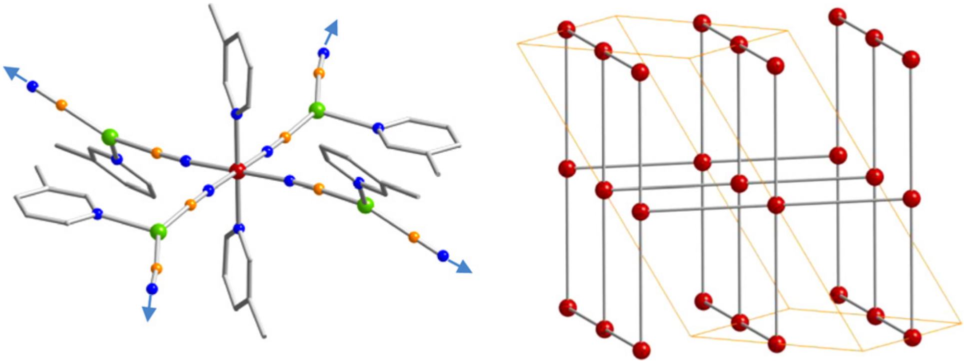

Fig. 4. Structure of **Cu3Clpy** (β-polymorph): Coordination surroundings of the Fe(II) and Cu(I) centers (left) and schematic view of the generated $CdSO_4$ 3D framework (right). Color code: Fe (red), Cu (green), N (blue), and C (orange), Cl (not shown).

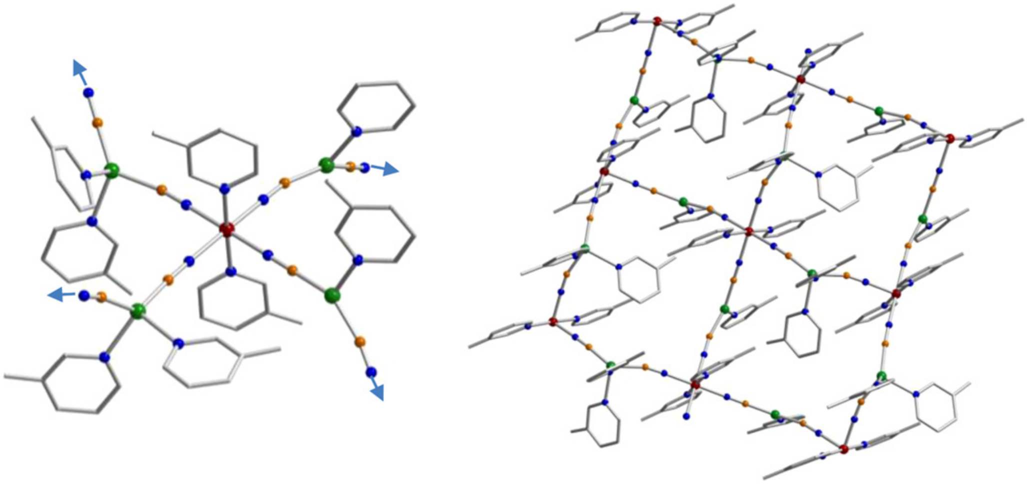

Fig. 5. Structure of **3FpyCu**: Coordination surroundings of the Fe(II) and Cu(I) centers (left). Color code: Fe (red), Cu (green), N (blue), C (orange), and Cl (not shown).

ogy of $CdCl_2$ (Fig. 6). The layers stack in such a way that generate short interlayer Cu···Cu distances, 2.5329 Å (293 K), indicating the presence of metallophilic interactions.

2.2. Spin crossover behavior

Compounds **3FpyCu**, **3ClpyCu** (β-polymorph), **Cu3CNpy**, and **Cupmd** undergo SCO behavior. They show typical Fe–N bond length variations (ca 0.20 Å) accompanied by significant angle variations (3–8°) in the Fe–N–C–Cu linkages. Furthermore, in **3FpyCu**, β-**3ClpyCu** derivatives the coordination bond lengths of Cu(I) display noticeable dependence (0.02–0.06 Å) upon SCO suggesting strong coupling between the Fe(II) ions and the $[Cu(CN)_2]^-$ bridging moieties. This flexibility in the coordination sphere of the Cu(I) site combined with the structural changes associated to Fe(II) derived from the SCO are reflected in the large change of unit cell volume, per Fe(II) atom, observed for **3FpyCu** ($\Delta V_{HL} = 50.7$) and β-**3ClpyCu** ($\Delta V_{HL} = 59$ Å^3) [9]. The noticeable ΔV_{HL} change found in **Cu3CNpy**

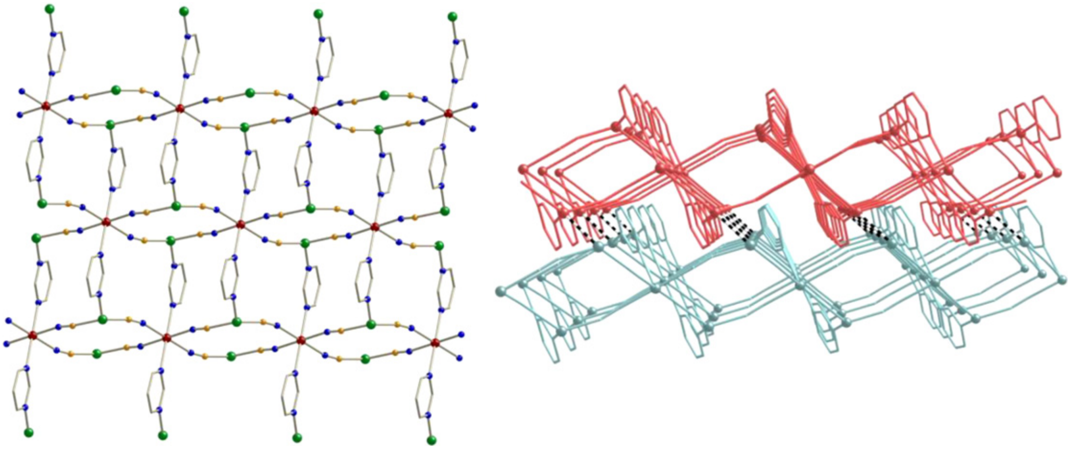

Fig. 6. Structure of **Cupmd**. Layer with the $CdCl_2$ topology (left). Two adjacent layers showing the Cu···Cu interactions (black and white bonds) (right). Color code: Fe (red), Cu (green), N (blue), and C (orange).

(46.2 Å^3) has been ascribed to the large variation (0.045 Å) of the interchain Cu$\cdots$Cu distances also associated with the spin conversion [8]. For **Cupmd**, ΔV_{HL} = 21.8 Å^3 is in the interval usually observed for most Fe(II) SCO compounds. In this compound, the Cu$\cdots$Cu separation is only moderately affected by the SCO since it decreases 0.0140 Å between the HS and the LS state [10].

The magnetic properties show moderate degree of cooperativity for **3FpyCu**, β-**3ClpyCu** and **Cu3CNpy** but no hysteretic behavior. This could be attributed to the flexibility of the Cu(I) coordination sphere. **3FpyCu** shows an irreversible phase transition that deeply affects its SCO properties. In a first cooling warming cycle, the magnetic data confirm that 19% of the iron atoms are in the HS state at 293 K, a value that reversibly decreases up to 8% at 130 K. This spin-state change is accompanied not only by an expected variation of the Fe–N bond distance (0.021 Å), but also by remarkable Cu–C and Cu–N(3Fpy) bond length variations. The former increases 0.022 Å while the latter decreases 0.037 Å. At temperatures above ca 310 K, a fast increase of the HS molar fraction denotes the occurrence of an irreversible SCO (T_c = 356 K). A second cooling warming cycle in the temperature interval 390–130 K denotes de occurrence of an atypical reversible SCO which present two different SCO regimes, a very continuous in the high temperature region involving ca 30% of iron atoms and other more abrupt in the low temperature region characterized by T_c = 187 K (Fig. 7). No evidence of crystallographic phase transition is observed after analyzing the structure at 293 K. The main structural changes arise from the bond angles and distances of the Fe(II) coordination sphere since the new phase contains 75% of iron(II) ions in the HS state at this temperature. Furthermore, noticeable bond angles and lengths are observed in the coordination surroundings of copper(I) showing again a certain degree of flexibility and strong coupling with the SCO centers. β-**3ClpyCu** displays a not well-defined two-step SCO (T_{c1} = 210 K and T_{c2} = 169 K), a fact that agrees with the presence of two slightly different [FeN$_6$] coordination spheres. For **Cu3CNpy** the critical temperature is T_c = 172 K [9].

The more rigid 2D system **Cupmd**, whose layers stack in a 3D system held by Cu$\cdots$Cu interactions (Fig. 6 left), displays a cooperative SCO characterized by a hysteresis loop 10 K wide with critical temperatures $T_c^{down} = 132$ K and $T_c^{up} = 142$ K. Quantitative photoinduction of the HS state occurs at 5 K (λ = 550 nm). Rapid relaxation of the photo-generated HS state to the stable LS state occurs at temperatures higher than 60 K (Fig. 8). The effect of pressure on the thermal induced SCO has also been carried out for this compound. As expected, pressure pushes the critical temperatures upward stabilizing the LS state decreasing at the same time the slope of the SCO curve and the hysteresis width [10].

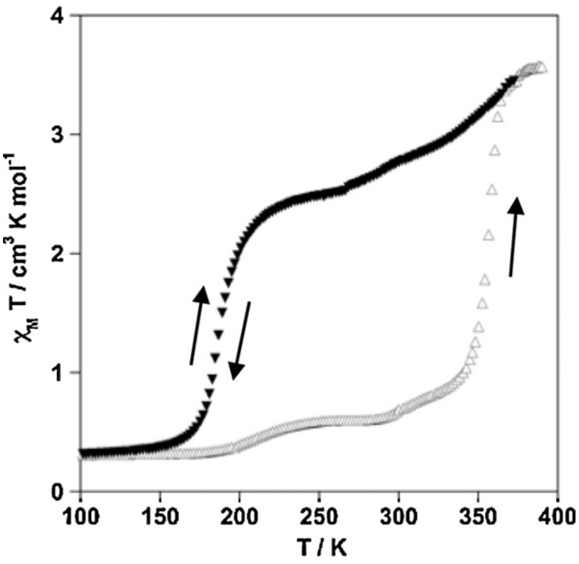

Fig. 7. Magnetic properties of **3FpyCu** (χ_M = magnetic susceptibility and T = temperature).

3. Dicyano-argentate and dicyano-aurate complexes

Like the dicyanocuprate complexes, the dicyanoargentate and dicyanoaurate counterparts also display the same structural principle by which the equatorial positions of the [FeN$_6$] octahedron are occupied by four [M(CN)$_2$]$^-$ bridging ligands while the axial positions are occupied by monodentate or bismonodentate pyridine-like ligands. However, the tendency to expand the coordination sphere of [M(CN)$_2$]$^-$ is strongly mitigated since chemical stability of M increases. Indeed, the [Ag(CN)$_2$]$^-$ ion has little tendency to *in situ* generate [Ag(L)$_n$(CN)$_2$]$^-$ species during the diffusion process in solution. Nevertheless, expansion of the coordination number of [Ag(CN)$_2$]$^-$ seems to be more commonly observed in the solid state in the presence of bismonodentate ligands. No examples of this phenomenology have been observed for [Au(CN)$_2$]$^-$ yet, most likely due to, in part, the persistent presence of metallophilic interactions.

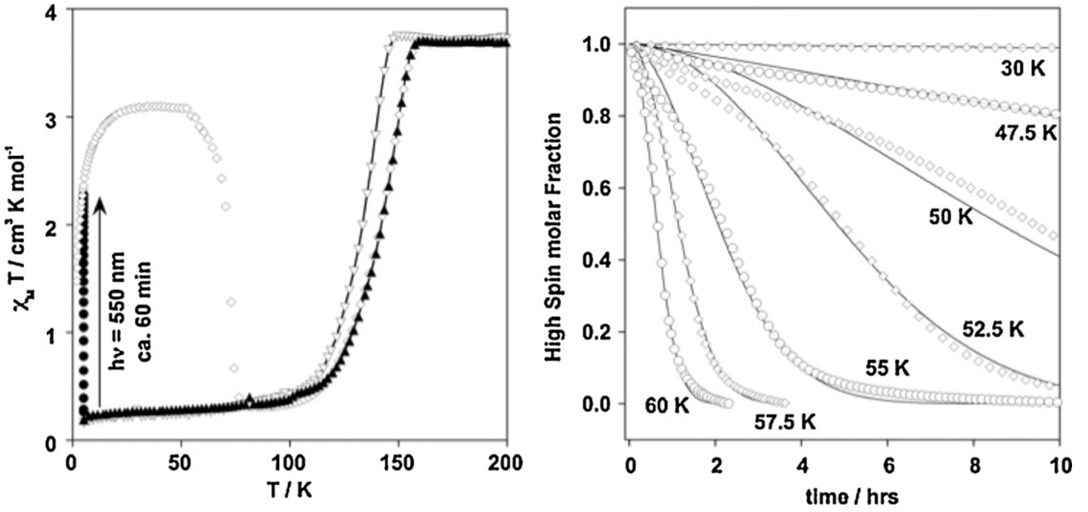

Fig. 8. Magnetic and photo magnetic properties of **Cupmd** (χ_M = magnetic susceptibility and T = temperature) (left). Relaxation of the photo-generated HS state (solid lines correspond to calculated values).

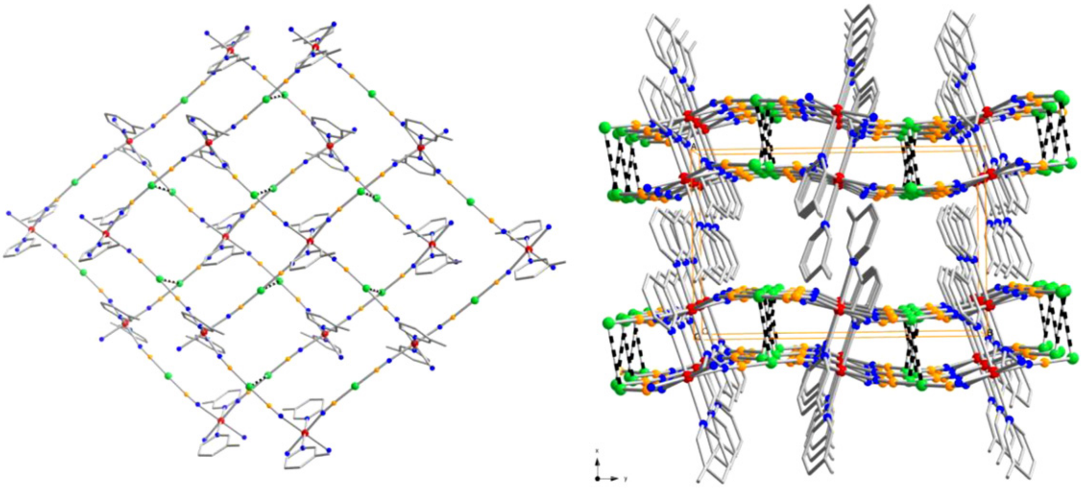

Fig. 9. 2D grids made up of edge-sharing $\{Fe[M(CN)_2]\}_4$ motives (left). Stacking of the layers showing strong metallophilic M···M interactions (black and white bonds). Color code: Fe (red), M (green), N (blue), and C (orange).

3.1. Pyridine based derivatives

3.1.1. 3-Halogenopyridines

3.1.1.1. Structure. The structural variety displayed by the halogen derivatives in $\{Fe(3Xpy)_2[Cu(3Xpy)_n(CN)_2]_2\}$ contrasts with the structural uniformity observed for the Ag and Au series, generically formulated $\{Fe(3Xpy)_2[M(CN)_2]_2\}$ (X = H, F, Cl, Br and I) abbreviated **M3Xpy**, whose structures are closely related. In the latter series the $[M(CN)_2]^-$ bridges remain practically lineal and, consequently, connect pairs of pseudoctahedral Fe(II) sites defining 2D grids made up of edge-sharing $\{Fe[M(CN)_2]\}_4$ motives (Fig. 9 left). The grids are organized in such a way that the iron atoms of one layer are below/above the center of the windows defined by the other layers. The layers are arranged in pairs. The separation between two layers in a pair is in the range 3.0–3.2 Å, indicating the occurrence of strong argentophilic or aurophilic interactions. This separation is about half of that observed between two consecutive layers of different pairs (Fig. 9 right) [11].

In situ generation of $[Ag(3Xpy)(CN)_2]^-$ species has been observed to occur in presence of excess of 3Brpy or 3Ipy giving $\{Fe(3Xpy)_2[Ag(CN)_2][Ag(3Xpy)(CN)_2]\}\cdot 3Xpy$ (**Ag3Xpy***) [11a]. Both Br and I derivatives are isostructural. These noncentrosymmetric compounds combine two different bridging $[Ag(CN)_2]^-$ and $[Ag(3Xpy)(CN)_2]^-$ units, which define slightly corrugated layers (Fig. 10 left). Unlike **Ag3Xpy**, the layers are regularly distributed and separated by ca 8 Å. The space between the layers is partially occupied by 3-Brpy or 3-Ipy guest molecules. Consequently, no argentophilic interactions are observed (Fig. 10 right). The guest 3-Xpy molecules interact via π-stacking with the coordinated ones defining infinite chains. Furthermore, there also are weak X···X contacts between the three types of 3-Xpy molecules. Another remarkable feature, which differentiates these compounds from the pale-yellow **Ag3Xpy** compounds, is the short Fe–N distances (observed for the 3-Ipy derivative), indicating that the former contains a noticeable number of Fe(II) ions in the LS state at temperatures close to 300 K, a fact that explains the red color that these compounds exhibit at room temperature.

No homologous gold compounds have been reported. However, the presence of an excess of 3-Ipy favors its inclusion during the diffusion process. Nevertheless, unlike the silver **Ag3Xpy*** derivative, the double layer structure remains intact in the resulting **Au3Ipy·(3Ipy)$_{0.5}$** compound (Fig. 11) [11b]. Most likely the well-known greater efficiency of aurophilic interactions and inert character of the $[Au(CN)_2]^-$ ions to expand their coordination sphere are the reasons that explain the observed structural differences. Furthermore, strong N → I donor–acceptor interactions occur between the nitrogen and iodine atoms of the guest and the coordinated 3-Ipy, respectively. The N···I distance is 2.994(7) Å at 293 K and decreases down to 2.907(5) Å at 80 K. These interactions are quite significant if we compare them with the strong N···I interactions reported for the infinite chains 4,4′-bipyridine/1,4-diiodobenzene or diiodotetrafluoroben-

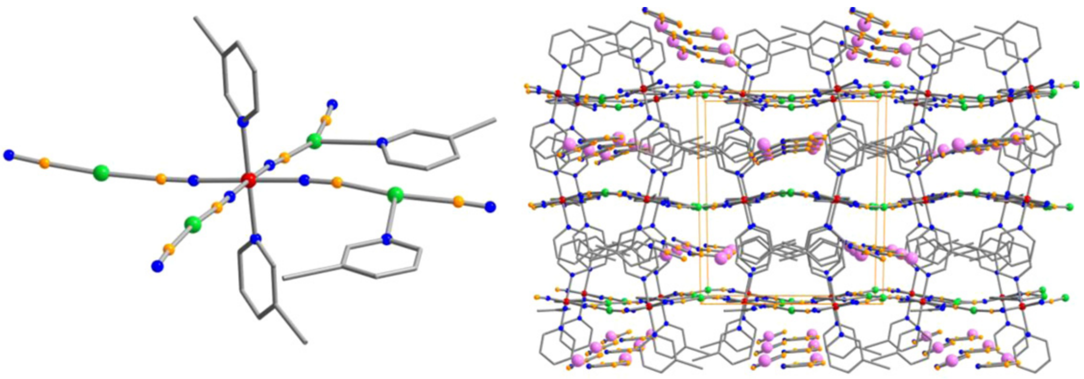

Fig. 10. Structure of **Ag3Xpy*** (X = Br, I): coordination surroundings of Fe(II) and Ag(I) (left), and crystal packing displaying the invited 3-Xpy molecules between the layers (right). Color code: Fe (red), Ag (green), N (blue), C (orange), and X atom of invited molecule (pink).

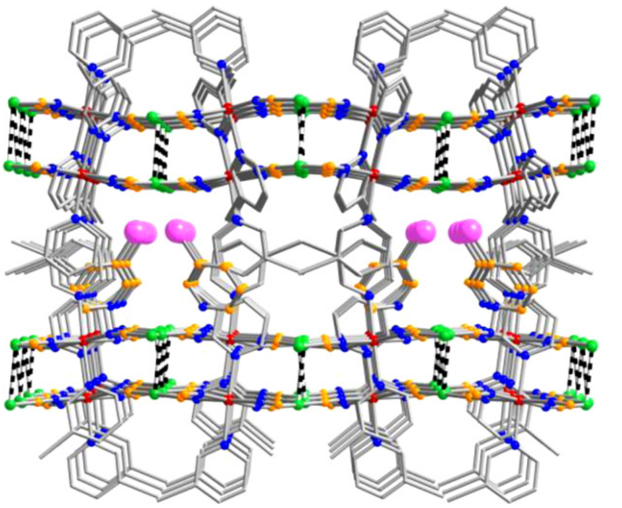

Fig. 11. Crystal packing of **Au3Ipy·(3Ipy)$_{0.5}$** showing the double layer structure and the invited 3-Ipy molecules. Color code: Fe (red), Au (green), N (blue), C (orange), and I atom of invited molecule (pink).

zene [12]. The N···I distances (and interaction energy) are 3.032 Å (13.19 kJ mol^{-1}) and 2.851 Å (24.32 kJ mol^{-1}), respectively, for these two systems.

3.1.1.2. *Spin crossover behavior.*

Ag3Fpy, **Ag3Clpy**, **Ag3Hpy** and **Au3Fpy** are the only spin crossover compounds in the **M3Xpy** series, the remaining compounds [M = Ag; X = Br, I) and (M = Au; X = H, Cl, Br, I)] are HS. Compound **Ag3Fpy**, displays a poor cooperative two-step transition with characteristic temperatures $T_{1/2}$ = 162 K and 96 K, reflecting the occurrence of two crystallographically distinct Fe(II) sites (Fig. 12a). This SCO behavior compares well with that reported for the unsubstituted homologue **Ag3Hpy** characterized by $T_{1/2}$ = 146.3 K and $T_{1/2}$ = 91 K [13]. A more steeper 50% ST taking place at relatively low temperatures, $T_{1/2}$ = 106 K, has been observed for **Ag3Clpy** in agreement with the average Fe–N bond distance and the crystal volume change at 100 K (Fig. 12a). For this compound only one type of Fe(II) site, averaged between the HS and LS states, has been observed [11a].

Two different SCO behaviors have been described for the system **Au3Fpy**. One displays a half spin transition characterized by an asymmetric hysteresis loop 5 K wide at an average critical temperature $T_c^{av} = 142.5$ K (Fig. 12b). At room temperature the crystals adopt the monoclinic $P2_1/c$ space group characterized by one crystallographically Fe(II) site in the HS state. At 120 K, the crystals display the triclinic *P*-1 space group where two crystallographically different but equally populated Fe(II) sites, one LS and the other HS, are observed [11b]. The second SCO behavior shows a complete two-step spin transition with critical temperatures T_{c1} = 147.9 K, $T_{c2}^{down} = 98.2$ K and $T_{c2}^{up} = 118.6$ K [14]. The fully LS crystal structure of this "second" form solved at 80 K shows that it recovers the monoclinic $P2_1/c$ space group. Although the magnetic behavior of these samples suggests the existence of two polymorphs, it is difficult to justify them from a crystallographic viewpoint. Application of relatively low pressures on the half SCO crystals induces a complete two-step spin conversion. At 0.16 GPa the low-temperature step clearly resembles that observed for the second sample (Fig. 12b).

Comparison of the spin transition behavior evidences a clear down shift tendency of the critical temperatures when moving from silver to gold. The same tendency was noted for two different series of isostructural compounds, {Fe(pyrimidine)(H$_2$O)[M(CN)$_2$]$_2$}·H$_2$O and {Fe(3CNpy)$_2$[M(CN)$_2$]$_2$}·2/3H$_2$O (M = Ag and Au) (vide infra). This has been explained in terms of higher electron affinity of gold with respect to silver. A stronger electron withdrawing (polarizing) effect over the CN groups, and hence a poorer donor capacity of the nitrogen atoms, is expected to occur in the [Au(CN)$_2$]$^-$ anions. This in turn is reflected in a decrease of the ligand field strength at the [FeN$_6$] site for the Au derivatives with respect to their Ag counterparts [11].

An intriguing aspect of these series is the apparent weakening of the ligand field strength around Fe(II) as the electronegativity of the halogen atom of 3-Xpy decreases. By the same simple electronic considerations used above, one should expect a decrease of the critical/characteristic temperature of the spin transition as the electronegativity of the axial ligand 3-Xpy (X = F, Cl, Br, I) increases. However, it has been suggested that the observed trend could be described in terms of the effective ligand field strength felt by the Fe(II) ions in the crystal, which takes into account the internal chemical pressure generated by the lattice. This chemical pressure can be "absorbed" more efficiently when highly polarizable atoms are present in the crystal as they can respond more readily to the strain changes in the lattice. In this respect, the presence of dominant X···X contacts shorter than the sum of the corresponding van der Waals distances between consecutive double layers may be a relevant factor to justify the trend in SCO critical temperatures observed for the **M3Xpy** series [11]. Of course, chemical pressure in molecular materials is still a rather ambiguous concept difficult of evaluate as it depends on many contributions (electrostatic interactions, hydrogen bonds, π–π interactions, etc.).

The paramagnetic behavior observed for **Ag3Xpy** (Br or I) strongly contrasts with the near room temperature SCO regime found for **Ag3Xpy*** ($T_{1/2} \approx 306$ K for X = Br and $T_{1/2} \approx 275$ for *X* = I, Fig. 12c). A similar situation is observed for the paramagnetic compound **Au3Ipy** and its related 3Ipy inclusion derivative **Au3Ipy·(3Ipy)$_{0.5}$**. The latter displays a two-step transition at much lower temperatures (T_{c1} = 155 K; $T_{c2}^{down} = 97$ K and $T_{c2}^{up} = 110$ K, Fig. 12c). These results suggest that the 3-Xpy guest molecules play an important role in the stabilization of the LS spin state. This is particularly true for the gold derivative since the composition and the double layer structure of the host framework remains essentially unchanged in the presence of the invited molecules.

3.1.2. *3-Cyanopyridine*

3.1.2.1. *Structure.*

Two isostructural SCO-CPs formulated {Fe(3CNpy)$_2$[M(CN)$_2$]$_2$} 2/3H$_2$O (M = Ag or Au) (**M3CNpy·2/3H$_2$O**) have been obtained from slow evaporation of Fe-3CNpy-[Au(CN)$_2$]$^-$ solutions in MeOH/H$_2$O (1:1) [15]. They form a four-connected 3D network with the prototypal NbO structure decorated by 3CNpy groups (Fig. 13 left). Triple interpenetration of identical {Fe[M(CN)$_2$]$_2$}$_\infty$ NbO-like structures occurs in both systems due to the open nature of this framework and the particular disposition of the coordinated 3CNpy groups (Fig. 13 right). They display cross-sectional trigonal and hexagonal channels when looking at along [0 0 1] direction. The vertices and edges of the trigonal channels are defined by the Fe(II) atoms and the [M(CN)$_2$]$^-$ groups, respectively. Each vertex is shared by an equivalent trigonal motif defining large hexagonal spaces partially filled with the 3CNpy groups, which form channels. These channels make ca. 6–7 Å in diameter and are occupied with water molecules. M^I···M^I intermetallic interactions are present in the triangular motifs (Fig. 14). The Ag···Ag distance is 3.256(2) Å (240 K) in the HS state and decreases 0.0967 Å (145 K) in the LS form. A much more moderate Au···Au contact was observed for the gold derivative in the HS state [3.4212 Å, 293 K]. This contact changes almost insignificantly [3.3952 Å, 120 K] upon spin conversion where only 30% of iron ions undergo SCO (vide infra) [15].

Evaporation of Fe-3CNpy-[Au(CN)$_2$]$^-$ solutions in MeOH/H$_2$O (1:1) also afford in much lower yield crystals of what can be considered as two unsolvated structural isomers, **Au3CNpy**, so called

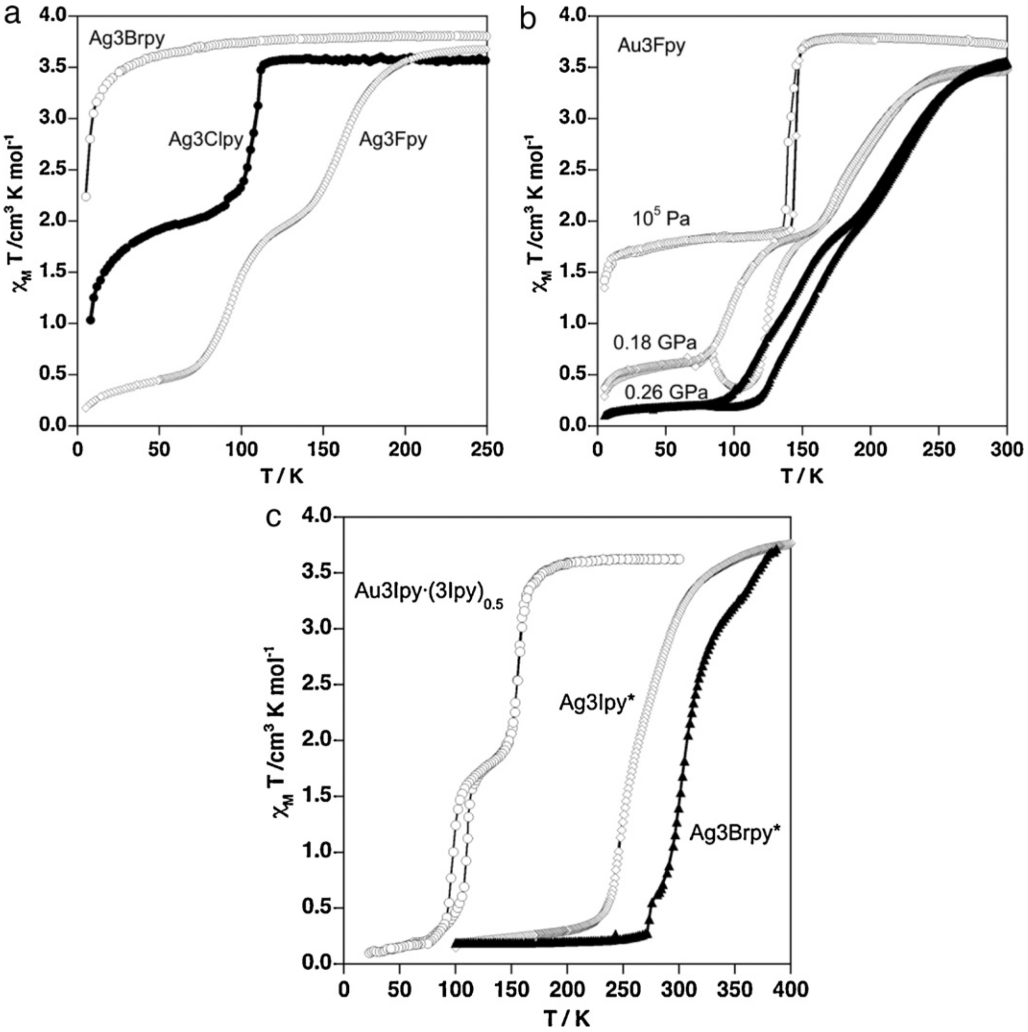

Fig. 12. Magnetic properties of **3XpyAg** (X = F, Cl, Br) (a), Au3Fpy at 10^5 Pa 0.18 and 0.26 GPa (b), and **Au3Ipy·(3Ipy)$_{0.5}$** and **Ag3Xpy*** (X = Br, I) (c) (χ_M = magnetic susceptibility and T = temperature).

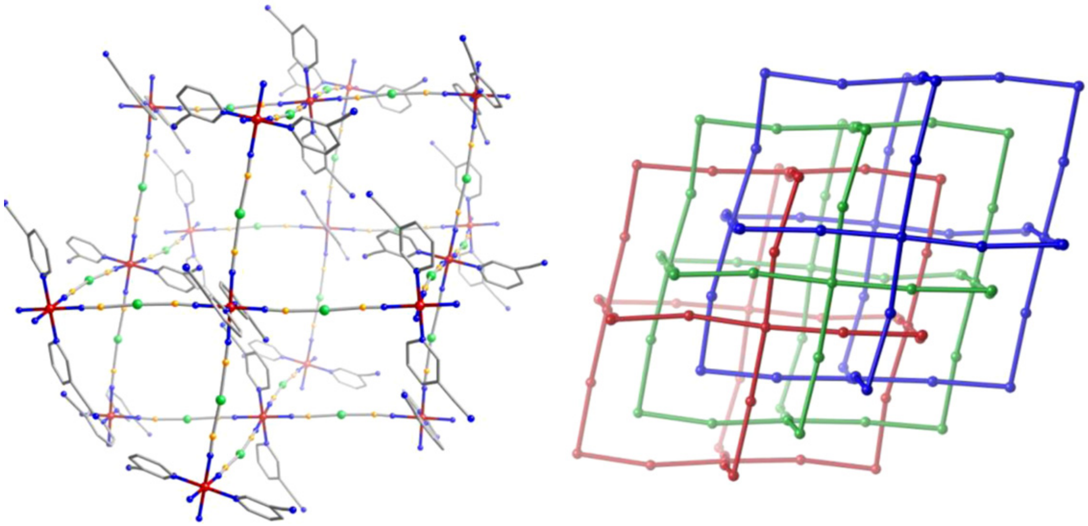

Fig. 13. Fragment of the structure of **M3CNpy·2/3H$_2$O** displaying the NbO-like topology (left) and the triple interpenetration of identical frameworks (right). The water molecules have been removed for sake of simplicity. Color code: Fe (red), M (green), N (blue), and C (orange).

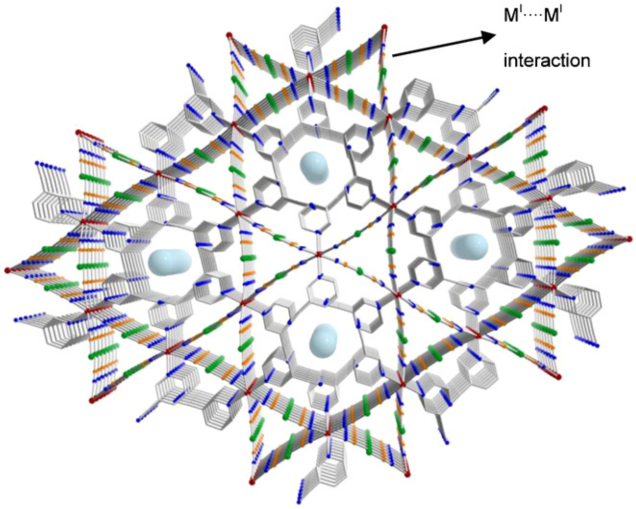

Fig. 14. View of the structure of **M3CNpy·2/3H$_2$O** along *c*-axis displaying the trigonal and hexagonal channels where M···M contacts take place and where the water molecules are located, respectively. Color code: Fe (red), M (green), N (blue), C (orange), and H$_2$O (light-blue).

polymorphs α and β [15b]. Both are constituted of 2D CPs. One of them has the double layer structure described for **M3Xpy** (Fig. 9) with short Au···Au contacts [3.1060(7) Å], which practically remain constant upon SCO (polymorph α). The second form is made up of a homogeneously distributed stack of layers, which do not show aurophilic interactions, polymorph β (Fig. 15).

When the Fe-3CNpy-[Au(CN)$_2$]$^-$ solutions are prepared essentially in MeOH, with a minimum amount of water to solubilize KAu(CN)$_2$, the formation of a new 2D CP formulated {Fe(3CNpy)$_2$(CH$_3$OH)$_{2/3}$[Au(CN)$_2$]$_2$} (**Au3CNpy/CH$_3$OH**) is favored [16]. The 2D CP is constituted of three independent Fe(II) centers. Fe(2) sites define the nodes of a slightly corrugated 2D grid while the octahedra defined by sites Fe(1) and Fe(3), rotated ca 90° with respect to site Fe(2), act as bismonodentate rods. Thus, two [Au(CN)$_2$]$^-$ groups in site Fe(1) are oriented almost perpendicularly to the surface of the layer and act as terminal ligands (Fig. 16 left). These long [Fe(1)–NC–Au–CN] arms penetrate the [Fe(2)]$_4$ windows of the adjacent layers in such a way that the peripheral N atoms of a particular layer, i.e. L(1), strongly interact via hydrogen bonding with the OH group of the CH$_3$OH molecules coordinated to the Fe(3) belonging to the layers L(1 ± 3) [N···O = 2.65 Å]. Layers L(2) and L(3) interact in the same way with L(2 ± 3) and L(3 ± 3), respectively. These interactions generate triple interpenetrated supramolecular 3D networks with the NbO topology (see Figs. 13 and 16 right). This compound is, in fact, precursor of the compound **Au3CNpy 2/3H$_2$O** discussed above. The reversible loss of the coordinated methanol molecules and the concomitant coordination of the terminal N atom to the Fe(3) site involves a change from the triclinic *P*-1 space group to the trigonal *P*-3 space group. Consequently, the 2D layers connected via hydrogen bonds convert into a rigid polymer made up of triple interpenetrated 3D coordination networks preserving the NbO topology. This process requires noticeable contraction of the space between the layers of ca. 2.371 Å and drastic reorientation of the aromatic rings, a fact that enables the formation of a hexagonal array of open channels shown in Fig. 14. These reversible structural changes affect noticeably the critical temperature of the spin transition observed for this compound (see below).

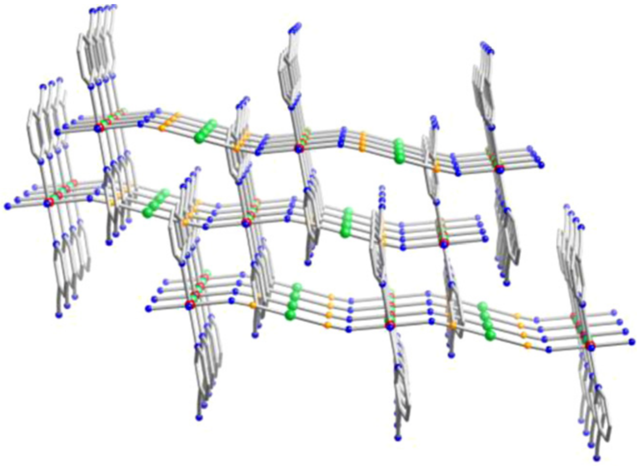

Fig. 15. Stacking of three consecutive layers of **Au3CNpy** (polymorph β). Color code: Fe (red), M (green), N (blue), and C (orange).

3.1.2.2. Spin crossover behavior. Compound **Ag3CNpy·2/3H$_2$O** undergoes a complete and moderate cooperative spin transition at T_c = 187 K characterized by a small step centered at 198 K which is clearly observed in the C_p versus *T* curve (Fig. 17). As expected, the average variation Fe–N bond length is ca. 0.2 Å upon SCO, however, the unit cell volume experiences a large variation, ca 45.05 Å^3. Similarly, the overall enthalpy and entropy variations, $\Delta H = 13.0 \pm 0.4\,\mathrm{kJ\,mol^{-1}}$ and $\Delta S = 69 \pm 3\,\mathrm{J\,mol^{-1}}$, are large regarding the cooperative nature of the transition. This likely reflects the occurrence of strong coupling between SCO and argentophilic interactions operating among the three interlocked independent 3D nets, indeed the Ag···Ag contacts change ca 0.1 Å upon SCO, as mentioned above [15a]. The isostructural Au counterpart undergoes an incomplete cooperative spin transition (ST) characterized by a hysteresis ca 6 K wide involving only 30% of the Fe(II) ions ($T_c^{\mathrm{down}} = 122$ K and $T_c^{\mathrm{up}} = 128$ K) [15b]. This incomplete ST seems to emulate the small step observed for the Ag derivative at much lower temperatures. Interestingly, pressure effect studies disclosed the appearance of two additional ST in **Au3CNpy 2/3H$_2$O** not observed at atmospheric pressure [17]. Another interesting concurrent fact is the large intermetallic Au···Au distances and their insignificant coupling with the SCO found in this compound compared with the silver homologue or even for other Au derivatives. However, it is difficult to assess whether the incompleteness of the ST, its transformation in a three-step ST under pressure in the gold derivative and the apparent two-step behavior in the silver compound are correlated with the structural features shown by these isostructural CPs.

Au3CNpy (polymorph α) undergoes a more cooperative 50% ST characterized by a hysteresis ca 13 K wide at lower temperatures ($T_c^{\mathrm{down}} = 107$ K and $T_c^{\mathrm{up}} = 120$ K) than **Au3CNpy 2/3H$_2$O**. This polymorph has a double layer structure tightly related to that of **Au3Fpy** which also displays 50% ST with critical temperatures ca 30 K higher (Fig. 4b). In contrast, polymorph β is paramagnetic in the whole range of temperature [15b].

The precursor compound **Au3CNpy/CH$_3$OH** displays a cooperative 30% ST at T_c = 169 K without hysteresis. After concerted substitution of the methanol molecules coordinated to Fe(3) sites by the terminal cyanide groups, the successor compound has, as expected, the SCO properties shown by **Au3CNpy·2/3H$_2$O**. Consequently, this reversible crystalline-state ligand substitution is accompanied by a decrease of the critical temperature of ca 44 K [16].

3.1.3. Methyl, phenyl and 4-(dimethyl/ethylaminostyryl) pyridines

The presence of methyl groups in the pyridine ligand has drastic consequences on the nature of the SCO behavior. For example, sub-

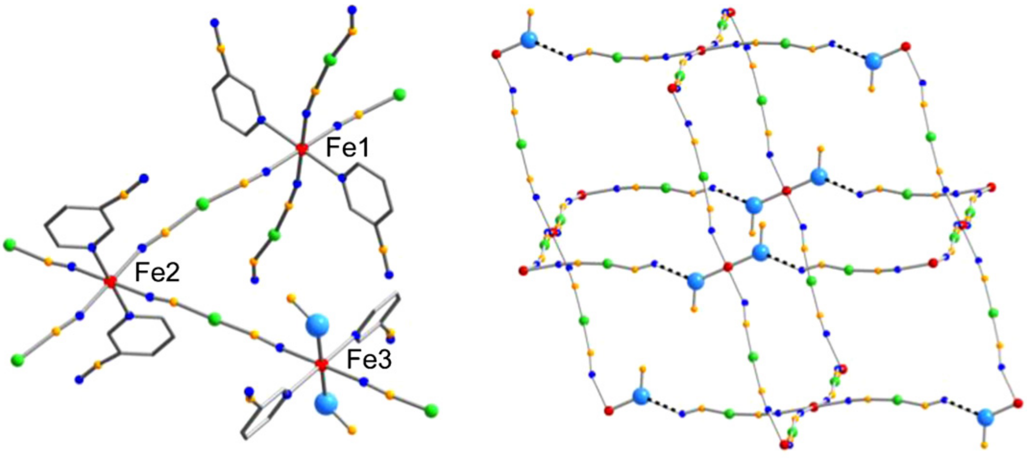

Fig. 16. Asymmetric unit of **Au3CNpy/CH$_3$OH** displaying the Fe atom numbering (left). Assembling of three layers via hydrogen bonding interactions (black and white bonds) defining the NbO-like topology (right). Color code: Fe (red), M (green), N (blue), C (orange), and O (blue).

stitution of the hydrogen atom in **Ag3Hpy** for a methyl group [13a] to afford **Ag3Mepy** provokes suppression of the spin SCO behavior since the latter compound is essentially in the HS state in the whole range of temperature [18]. In contrast, **Ag4Mepy** undergoes a gradual SCO centered at about 175 K over a broad temperature range of more than 150 K [18]. Although the structure of these methylated derivatives is unknown, it is expected to be similar to that of the homologous gold compound **Au4Mepy** [19], which has been structurally characterized. The latter compound displays typical double-layered structure sustained by strong aurophilic interactions already described for the 3-halogenpyridines (Fig. 9). This gold derivative undergoes an uncommon triple–step ST, which resembles that observed for **Au3CNpy·2/3H$_2$O** at pressures higher than 10^5 Pa.

The last member of this series is $\{Fe(3,5Mepy)_2[Ag_2(CN)_3][Ag(CN)_2]\}$ (**Ag3,5Me$_2$py**), which contains the 3,5-dimethylpyridine ligand. This compound is singular because $[Ag(CN)_2]^-$ partially converts into the lineal $[Ag_2(CN)_3]^-$ anion during the crystallogenesis process. It consists of three interpenetrated 3D frameworks with the topology of $CdSO_4$ (see Fig. 4 right). Inter-framework argentophilic interactions are observed, which strongly depend on the spin state of the iron (i.e. Ag···Ag = 3.224 Å (HS) to 3.073 Å (LS)). The magnetic behavior denotes the occurrence of a ST without hysteresis at T_c = 235 K [20].

Two series of pyridine ligands bearing bulky substituents have also been investigated. The synthesis and characterization of $\{Fe(4phpy)_2[M(CN)_2]_2\}\cdot nH_2O$ (M = Ag, n = 1; M = Au, n = 0.5), where 4phpy is 4-phenylpyridine, have been carried out as a preliminary step in the development of new liquid crystals based on 2D SCO-CPs [21]. No structural information is available for these compounds, which undergo relatively poor cooperative SCO behaviors with characteristic temperatures $T_{1/2}{}^1$ = 213 K and $T_{1/2}{}^2$ = 162 K for **Ag4phpy H$_2$O** and $T_{1/2}$ = 225 K for **Au4phpy 1/2H$_2$O**. After dehydration, the silver derivative displays a unique step at slightly higher temperatures ($T_{1/2}$ = 226 K).

Aiming at exploring synergies between SCO and non-linear optic (NLO) responses, the compounds $\{Fe(DMAS)_2[Ag(DMAS)(CN)_2]_2\}$ (**AgDMAS***) and $\{Fe(L)_2[M(CN)_2]_2\}$ (**ML**) (M = Ag or Ag) based on the stilbazole ligands L = 4-dimethylaminostilbazole (DMAS) or 4-diethylaminostilbazole (DEAS), have been investigated [22]. **AgDMAS*** is the only member of this series in which the silver atom expands the coordination number to give pseudotrigonal bridging units $[Ag(DMAS)(CN)_2]$. This fact together with the length of the DMAS ligand cause marked congestion between two consecutive parallel $\{Fe[M(CN)_2]_2\}_\infty$ grids, separated by 17.563(4) Å, where the

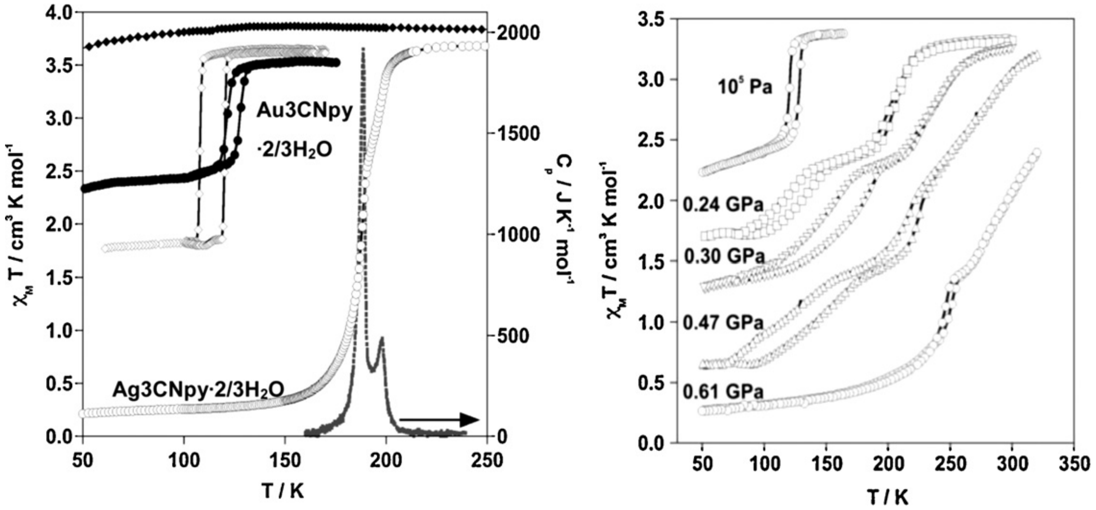

Fig. 17. (Left) Magnetic (open circles) and calorimetric (dotted line) data of **Ag3CNpy·2/3H$_2$O**. Magnetic properties of **Au3CNpy·2/3H$_2$O** (filled circles), **Au3CNpy** polymorphs α (open diamonds) and β (filled diamonds). (Right) Influence of pressure on the spin transition of **Au3CNpy·2/3H$_2$O** (χ_M = magnetic susceptibility, T = temperature, and C_p = anomalous molar heat capacity).

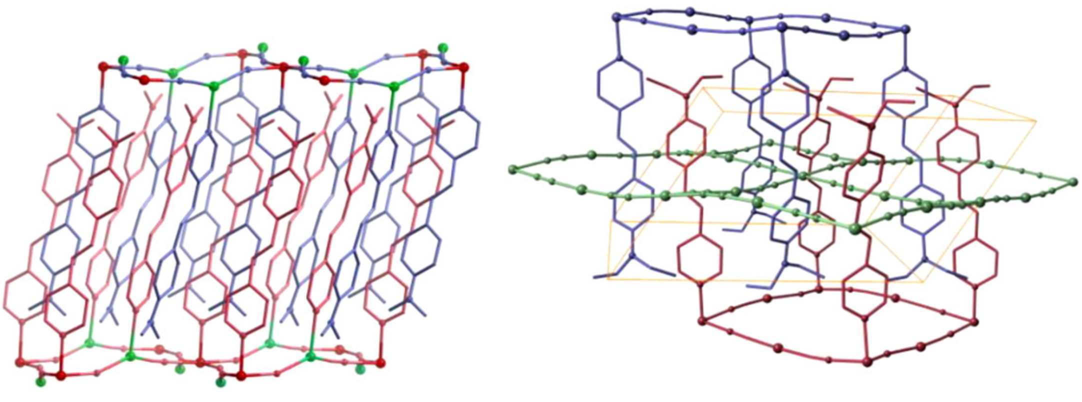

Fig. 18. Fragment of two consecutive layers of **AgDMAS*** showing ligand congestion between the layers (left). View of a fragment of **AgDEAS** illustrating the interpenetration of the layers (right).

DMAS ligands interdigitate (Fig. 18 left). In contrast, the lack of congestion in the remaining compounds of this series facilitates the long axial ligands to penetrate the windows of the $\{Fe[M(CN)_2]_2\}_\infty$ grids in such a way that two consecutive grids are around 9.8 Å apart (Fig. 18 right). **AgDMAS*** is a typical HS compound while **AgDEAS** represents a new example of a 33% cooperative ST with characteristic temperatures $T_c^{down} = 138$ K and $T_c^{up} = 144$ K. This ST is accompanied by a reversible crystallographic phase transition in which the unit cell almost doubles volume in the low temperature crystallographic phase. The lack of SCO in the former compound has been ascribed to its peculiar crystal packing since similar average Fe–N bond distances are observed for both DMAS and DEAS compounds. **AuDMAS** displays a gradual two-step SCO behavior with characteristic temperatures $T_{1/2}{}^1 = 226$ K and $T_{1/2}{}^2 = 132$ K. This strongly contrasts with the HS-to-LS change involving less than 5% of iron atoms in the temperature range 100–50 K observed for **AuDEAS**.

3.2. *Pyrimidine derivatives*

Self-assembly of $[M(CN)_2]^-$ (M = Ag, Au), pyrimidine (pmd), and iron(II) has generated an exceptionally rich variety of CPs with interesting structural, physical, and chemical properties: (i) $\{Fe(pmd)[Ag_3(CN)_2][Ag(CN)_2]\}$ (**Agpmd***) [23]; (ii) $\{Fe(pmd)_2[Ag(CN)_2]_2\}$ polymorph α (**Agpmd₂**-α) and polymorph β (**Agpmd₂**-β) [24]; (iii) $\{Fe(pmd)(H_2O)[M(CN)_2]_2\}$ H_2O (**MpmdH₂O**) (M = Ag, Au) [25]; (iv) $\{Fe(pmd)[M(CN)_2]_2\}$ (**Mpmd**) (M = Ag, Au) [25]. Furthermore, the complexes $\{Fe(5Brpmd)[M(CN)_2]_2\}$ (**MBrpmd**) (M = Ag, Au) where 5Brpmd is the 5-bromopyrimidine have also been investigated [26].

3.2.1. *Synthesis*

Concerning chemical diversity in the Fe-pmd-$[Ag(CN)_2]$ system, an intriguing question is how these compounds have been synthesized. Except for **Mpmd**, which was obtained from the dehydration of **MpmdH₂O**, the remaining polymers were isolated as single crystals from slow diffusion of water solutions in H-shaped vessels. Single crystals of **Agpmd*** and **AgpmdH₂O** apparently are strongly favored when temperature is kept below to 15 °C during the diffusion process. Usually, compound **AgpmdH₂O** appears the first as yellow polyhedral crystals while **Agpmd*** crystallizes as well-defined clumps of flattened pale-yellow prismatic crystals in the subsequent 2–4 weeks. Single crystals of **Agpmd₂**-α and **Agpmd₂**-β grow in diffusion vessels when temperature is kept at around 303 K together with small amounts of crystals of **AgpmdH₂O**). They are easily separated using a binocular lens, since have distinct colors, pale-yellow and orange-yellow for **Agpmd₂**-α and **Agpmd₂**-β, respectively. Given the insolubility of both polymorphs they can also be prepared by direct precipitation. However, only in a few cases, the samples consist in pure phases, since usually they precipitate as mixtures of both. The gold component **AupmdH₂O** is more conveniently obtained as pale-yellow single crystals from evaporation under an argon stream. The seven members of this series of polymers have been structurally characterized.

3.2.2. *Structure*

The structure of **Agpmd*** is rather singular [23]. Like the aforementioned **Ag3,5Me₂py** compound, it contains two anionic bridging ligands: $[Ag(CN)_2]^-$ and the uncommon species $[Ag_2(CN)_3]^-$ formed *in situ* during the crystallization process. However, the presence of the pmd bridging ligand determines the formation of an intricate self-interpenetrated 3D network.

There are five crystallographically independent iron atoms in the asymmetric unit two of which [Fe(4) and Fe(5)] are located on inversion centers. Thus, the asymmetric unit contains a total of four iron atoms: three full iron atoms [Fe(1), Fe(2) and Fe(3)] and half of Fe(4) and Fe(5). The equatorial bonds are defined by the nitrogen atoms of the $[Ag(CN)_2]^-$ and $[Ag_2(CN)_3]^-$ groups and are shorter than those of the axial bonds occupied by the nitrogen atoms of the pmd groups, which act as bridging ligands between iron centers, forming $-[Fe\text{-}pmd\text{-}Fe]_\infty-$ chains running along the *c* axis (Fig. 19). There are three different kinds of such chains in the structure (noted Fe(i)-pmd-Fe(j)): Fe(1)-pmd-Fe(1), Fe(2)-pmd-Fe(3) and Fe(4)-pmd-Fe(5). The chains Fe(1)-pmd-Fe(1) and Fe(4)-pmd-Fe(5) alternate along the direction of the *b* axis, defining layers of iron atoms lying in the *bc* plane. These layers alternate along the *a* axis with similar layers formed only of Fe(2)-pmd-Fe(3) chains (Fig. 19). Adjacent iron layers are connected through $[Ag(CN)_2]^-$ and $[Ag_2(CN)_3]^-$ bridges. A particular chain, i.e. Fe(2)-pmd-Fe(3), connects with four other chains (i.e. two Fe(1)-pmd-Fe(1) and two Fe(4)-pmd-Fe(5)) defining circuits with (6,6) topology, which radiate in different directions toward the surrounding chains (Fig. 19b and c). These circuits are interpenetrated by other circuits defined by adjacent $-[Fe\text{-}pmd\text{-}Fe]_\infty-$ chains and $[Ag(CN)_2]^-$ or $[Ag_2(CN)_3]^-$ groups. Interestingly, dense layers of Ag atoms sustained by strong argentophilic interactions separate the space between the iron layers. The shortest Ag···Ag distances, 2.98–3.02 Å, are slightly longer than that in Ag metal (2.89 Å).

Compounds **Agpmd₂**-α and **Agpmd₂**-β have the same chemical formula but different crystal structures [24]. They constitute a new example of architectural isomerism. These compounds can be viewed as 3D CPs made up of an infinite stack of $\{Fe_4[Ag(CN)_2]_4\}_\infty$ grids. The pmd groups, which lie in the iron(II) axial positions, interact with the silver atoms belonging to the adjacent layers, defining 3D architectures. The architectural isomerism represented by both α and β forms is associated with the conformational changes occur-

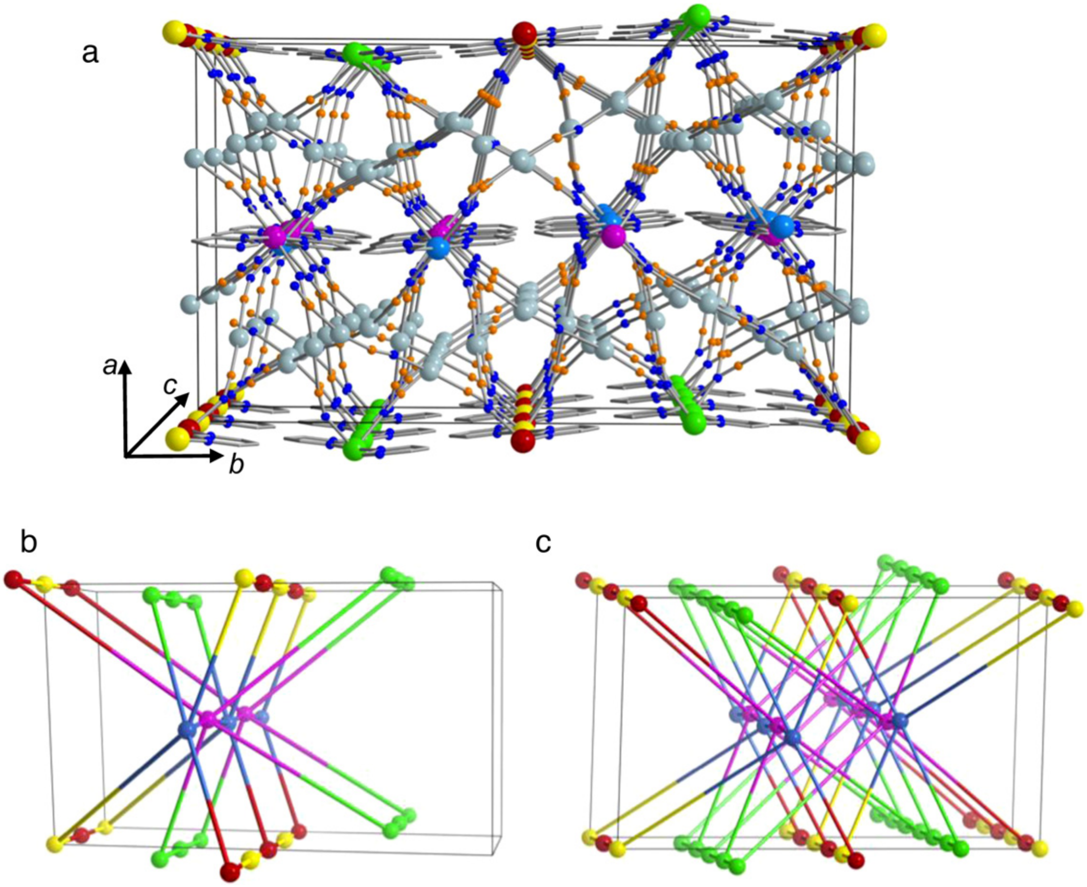

Fig. 19. Structure of **Agpmd*** displaying the intricate connectivity between different –[Fe(1)-pmd-Fe(1)]$_\infty$– chains running along *c*-direction (a). Schematic representations of the connectivity of a particular –[Fe(2)-pmd-Fe(3)]$_\infty$– chain with four –[Fe(1)-pmd-Fe(1)]$_\infty$– and four –[Fe(4)-pmd-Fe(5)]$_\infty$– chains belonging to adjacent Fe(II) layers (b) and to a complete unit cell (c), showing the (6,6) topology of the network and the interpenetration of the (6,6) circuits. Color code: Fe(1) (green), Fe(2) (blue), Fe(3) (pink), Fe(4) (red), Fe(5) (yellow), and Ag (grey).

ring in the $[Ag(CN)_2]^-$ ligands. More precisely, the $[Ag(2)(CN)_2]$ anion has an uncommon distorted bent geometry [C(5)-Ag(2)-C(5) = 138.8°] in **Agpmd$_2$**-α, which induces strong undulation of the $\{Fe[Ag(2)(CN)_2]_2\}_\infty$ chains and allows parallel interpenetration of two identical grids held together by strong argentophilic interactions (Ag···Ag distance is 2.9972 Å). This strong deviation from linearity is a consequence of the coordination of two peripheral nitrogen atoms of two pmd ligands belonging to a contiguous layer,

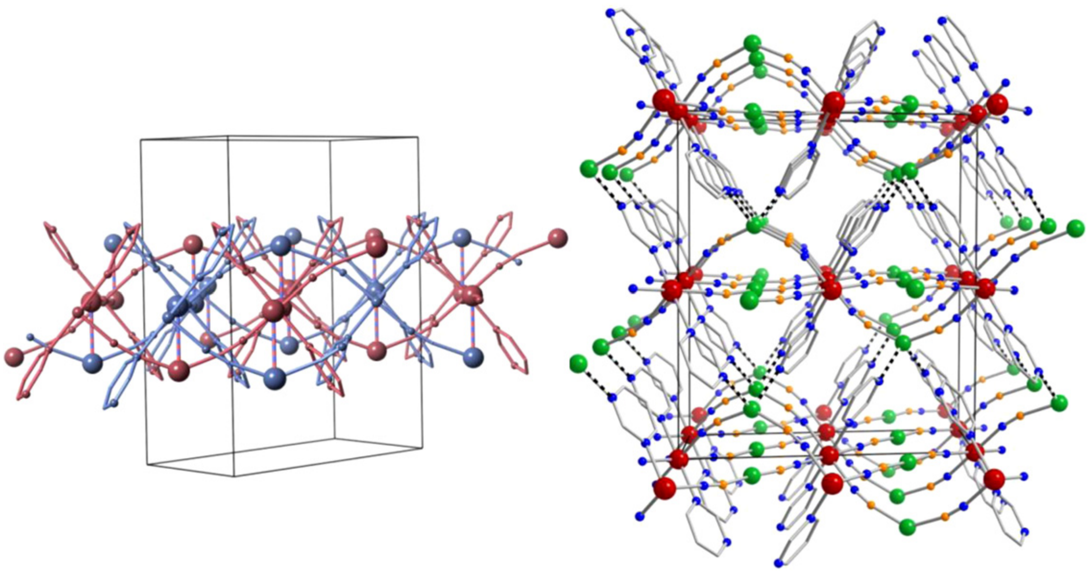

Fig. 20. Structure of **Agpmd$_2$**-α: View of two interpenetrated undulated layers (dotted lines represent strong Ag···Ag interactions between layers (left). Crystal packing of the double layers (dotted lines represent the coordinative interactions between pmd and $[Ag(2)(CN)_2]^-$) (right). Color code: Fe (red), Ag (green), N (blue), and C (orange).

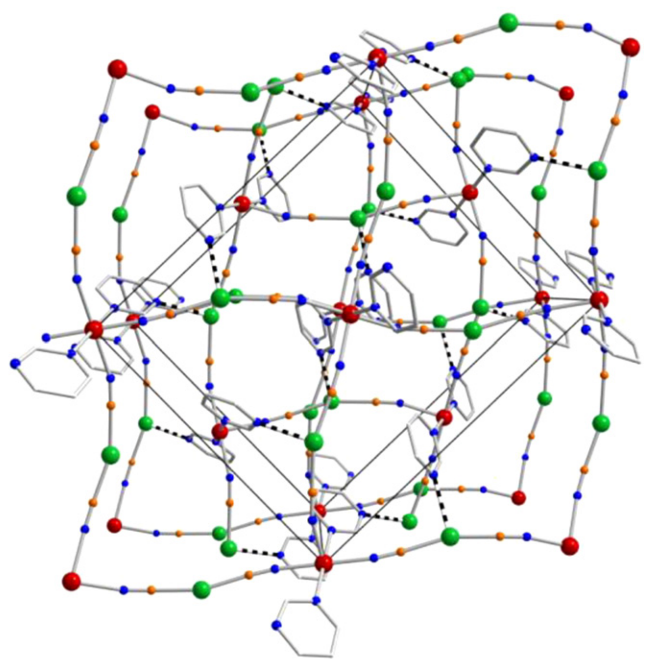

Fig. 21. Crystal packing of $\mathbf{Agpmd_2}$-β. The peripheral N atoms of the pmd ligands of one layer interact with the Ag atoms of the adjacent layer (dotted lines represents the resulting Ag-N bonds). Color code: Fe (red), M (green), N (blue), and C (orange).

which confers to the Ag(2) atom a distorted tetrahedral geometry (Fig. 20). In the polymorph β, the $[Ag(CN)_2]^-$ ligand is remarkably less bent [C(5)-Ag-C(6) = 161.8°], consequently, no interpenetration occurs. Connectivity between adjacent single layers takes place through coordination of the Ag atoms by the peripheral nitrogen atoms of the pmd ligands (Fig. 21).

Compounds $\mathbf{MpmdH_2O}$ with M = Ag, Au are isostructural and have two crystallographically distinct iron sites [25]. One, has two pmd rings coordinated in the axial positions, which act as monodentate ligands, whereas the other site has two water molecules coordinated in the axial positions. Both sites are connected in an alternate way describing an open 3D framework with the topology of $CdSO_4$ (Fig. 22a). Three identical nets interpenetrate to fill the empty spaces (Fig. 22b). The nets interact via hydrogen bonds and metallophilic interactions. The hydrogen bonds are formed between the coordinate water molecules of one net with the uncoordinated nitrogen atom of the pmd rings of the two adjacent nets (Fig. 22c). In addition, a 2D network of hydrogen bonds is established between the coordinated and the inclusion water molecules located in the channels.

Complete dehydration takes place at relatively low temperatures in only one step or under vacuum. This easy and reversible process resembles that described for $\mathbf{Au3CNpy{\cdot}2/3H_2O}$ and is assisted by a topochemical crystalline-state ligand substitution involving coordination/uncoordination of gaseous water and pyrimidine. This induces expansion/contraction of the nanoporous framework and the solid-state transformation of the three interpenetrated nets into a single 3D net (Fig. 22d).

Interestingly, the utilization of 5-Brpmd instead of pmd affords **MBrpmd** (M = Ag, Au), which has the structure of the dehydrated form **Mpmd**, namely, three interpenetrated networks with the $CdSO_4$ network topology interconnected by 5-Brpmd bridges.

3.2.3. Spin crossover behavior

Given the singular features of **Agpmd*** its thermal and light induced SCO properties have been investigated in depth combining magnetic and calorimetric measurements, single crystal absorption spectroscopy, detailed variable temperature crystal determinations and photo-crystallographic studies [23]. The magnetic properties feature a two-step ST involving each step ca. 50% of the Fe(II) sites with critical temperatures T_{c1} = 185 K and T_{c2} = 147 K (the low temperature step displays a narrow hysteresis of about 1.5 K). The thermodynamic parameters were evaluated from calorimetric measurements as $\Delta H_1 = 3.6 \pm 0.4\,\mathrm{kJ\,mol^{-1}}$, $\Delta S_1 = 19 \pm 3\,\mathrm{J\,K^{-1}\,mol^{-1}}$ and $\Delta H_2 = 4.8 \pm 0.4\,\mathrm{kJ\,mol^{-1}}$, $\Delta S_2 = 33.5 \pm 3\,\mathrm{J\,K^{-1}\,mol^{-1}}$ (Fig. 23). The two-step ST was also monitored using electronic spectroscopic

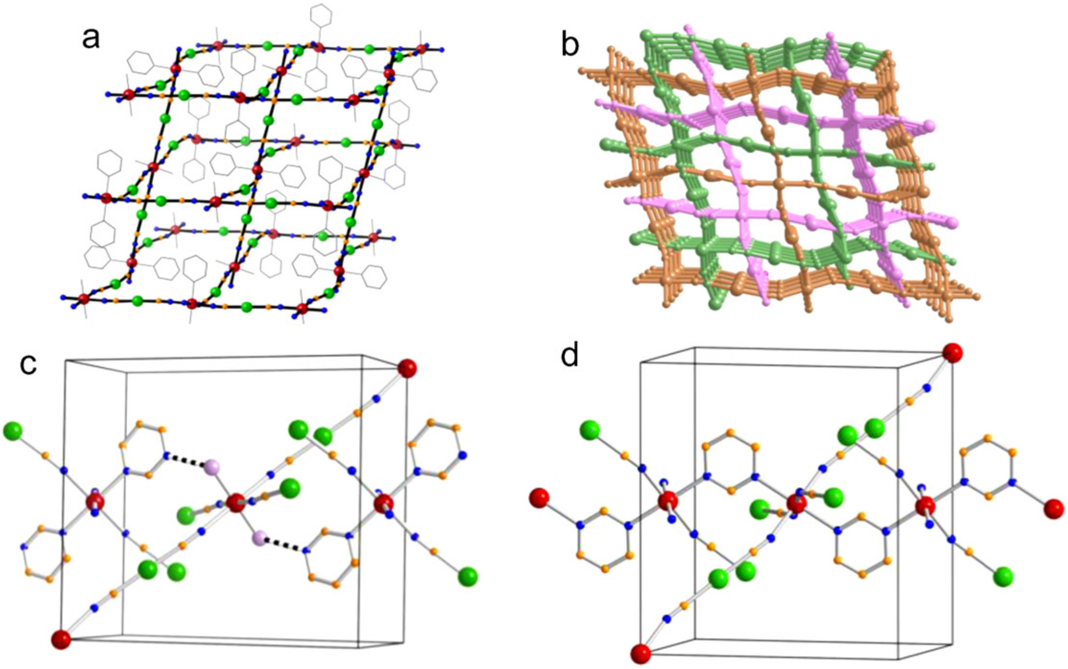

Fig. 22. (a) Fragment of the 3D network of $\mathbf{MpmdH_2O}$ displaying the topology of the $CdSO_4$ structure. (b) Perspective view of the three interlocked networks. (c) Unit cell showing fragments of three networks and their connectivity via hydrogen bonding (dotted lines). (d) Unit cell of the dehydrated species **Mpmd**. Color code: Fe (red), M (green), N (blue), C (orange), and O (pink).

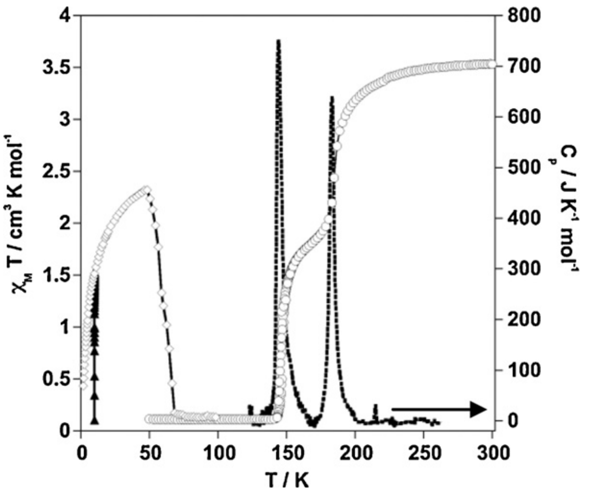

Fig. 23. Magnetic, photomagnetic, and calorimetric properties of **Agpmd***
(χ_M = magnetic susceptibility, T = temperature, and C_p = anomalous molar heat capacity).

studies in the visible region on single-crystal taking advantage of the color change which characterize the spin state change from yellow (HS) to deep red (LS), observed for most iron(II)-M cyanide based CPs. Fig. 24 shows the thermal evolution of the coefficient of molar extinction (ε) of **Agpmd*** in the cooling mode (left) and the corresponding thermal evolution of the estimated HS molar fraction (γ_{HS}) (right). The results from the bulk magnetic studies and single-crystal optical studies match well.

The crystal structure was studied at 290, 220, 170, 90, 30 and at 30 K after irradiation with red light (λ = 633 nm). The compound crystallizes in the monoclinic system ($P2_1/c$, Z = 16) and does not change symmetry irrespective of temperature and light irradiation. The structural motifs are essentially the same at all temperatures, with changes in bond lengths and angles in keeping with the characteristic structural changes of the spin transition. The main conclusions of this structural analysis are as follows: (i) At 290 K and at 90 K (30 K) all iron sites are in the HS state and in the LS state, respectively; (ii) the most susceptible iron site to undergo SCO is Fe(5) as it is the only one whose Fe–N bond lengths change appreciably in the temperature region 290–220 K; (iii) In the middle of the plateau (170 K) sites Fe(3) and Fe(5) are in the LS state while Fe(2) and Fe(4) are in the HS state, however, the average Fe–N bond lengths are in an intermediate situation between the HS and LS states for site Fe(1); (iv) Strong synergy is observed between SCO behavior argentophilic interactions. About ca. 60% of the Ag···Ag short contacts change significantly during the second step.

These data reveal that an alternating arrangement exists of –[HS-LS-HS]$_\infty$– states in the two chains formed by two inequivalent iron atoms in the plateau, namely –[Fe(2)-pmd-Fe(3)]$_\infty$– and –[Fe(4)-pmd-Fe(5)]$_\infty$–. Despite the diffraction technique only "sees" an average of the two states in Fe(1) site, it is reasonable to conclude that similar arrangement occurs in the –[Fe(1)-pmd-Fe(1)]$_\infty$– chains. Furthermore, there is an apparent correlation between the changes observed for the argentophilic interactions in each step and the entropy (ΔS) and unit cell volume (ΔV) variations. Indeed, 60% of the significant variations observed for the Ag···Ag contacts intensify during the low temperature step and accordingly ΔS_2 and ΔV_2 are ca. 40% and 11% larger, respectively, than ΔS_1 and ΔV_1. Synergy between metallophilic interactions and the SCO phenomenon has already been observed for the aforementioned CP **Ag3CNpy 2/3H$_2$O**.

Photo-magnetic and photo-optical studies show that the compound undergoes LIESST at low temperature. Relaxation of the sample at different temperatures (Fig. 25) shows that the iron atoms in the lattice can be divided into two groups from the point of view of the magnetic and optical behavior, in agreement with the diffraction results. Related to the two steps in the thermal transition curve, there are two distinctly different slopes seen in the relaxation curves and the first section of the relaxation is faster than the second section. Structural studies have led to the identification of the first iron center (Fe(5)) to undergo thermal spin crossover. Similar studies carried out at 30 K on the photo-excited state show that Fe(5) is in the LS state, the others remain trapped in the HS state. Thus the Fe(5) center appears to show the lowest activation barrier for the relaxation HS-to-LS and due to the nature of the diffraction experiment relaxes too fast to be measured at 30 K. A full thermodynamic and kinetic analysis of the spin transitions has been carried out from the direct observation of the thermal- and light-induced structural changes associated to each iron(ii) site, which have revealed for the first time the microscopic mechanism of a complex cooperative spin transition in a fascinating material.

Both architectural isomers **Agpmd$_2$**-α and **Agpmd$_2$**-β display quite similar average Fe–N$_{av}$ bond distances (2.190 Å α-form and 2.172 Å β-form). Despite this small difference, α-form is a HS compound in the whole range of temperature while β-form undergoes a cooperative ST characterized by $T_c^{down} = 181.1$ K and $T_c^{up} = 186.3$ K

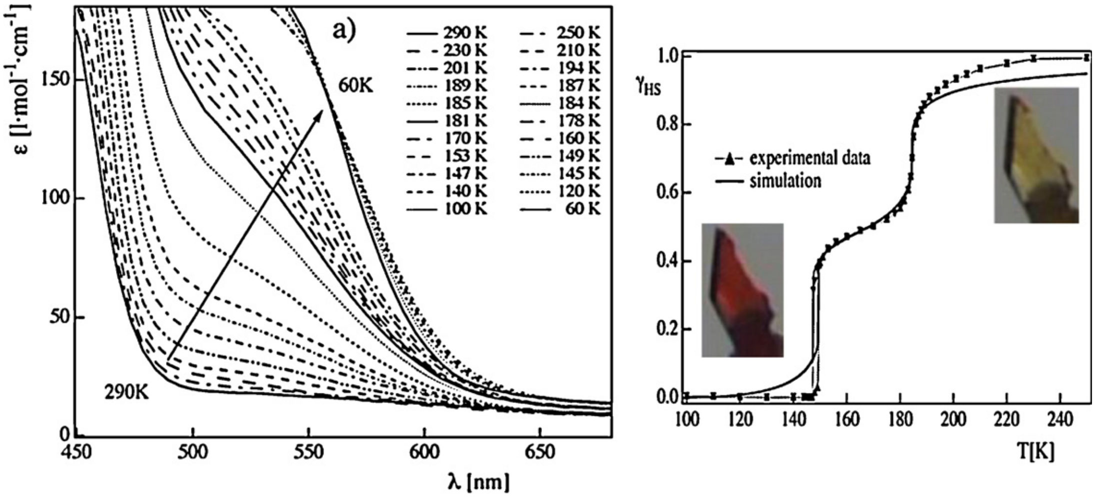

Fig. 24. Single crystal absorption spectra in the cooling mode (290–60 K) (left) and thermal spin transition curve obtained from optical measurements (right) of **Agpmd***. Inset: change of color of a single crystal.
Adapted from Ref. [23].

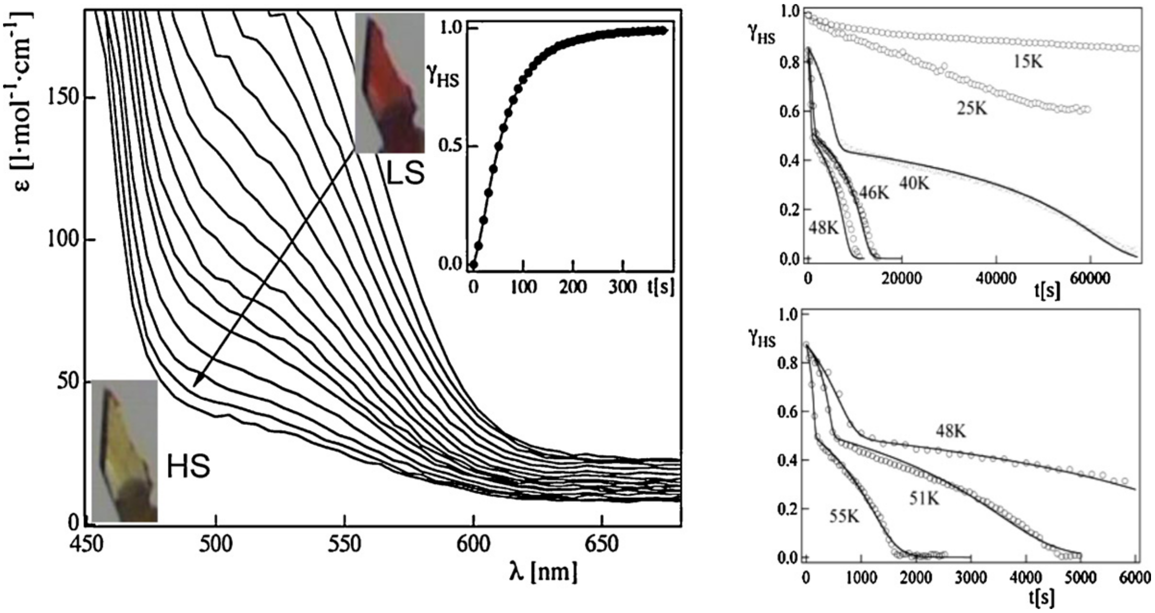

Fig. 25. (Left) Single crystal absorption spectra of **Agpmd*** obtained during photoexcitation at 10 K with 647 nm light (11 mW mm^{-2}). Inset: corresponding excitation curve and crystal color change. (right) HS → LS relaxation curves recorded at different temperatures from optical measurements following quantitative photo-excitation at 10 K. Solid line represents simulations.
Adapted from Ref. [23].

(ΔH_{av} = 11.2 ± 0.5 kJ mol^{-1}; ΔS_{av} = 62 ± 3 J K^{-1} mol^{-1}) (Fig. 25 left) [24].

The isostructural compounds **MpmdH$_2$O** (M = Ag, Au) display cooperative spin transitions with critical temperatures $T_c^{down} = 215$ and $T_c^{up} = 223$ K (ΔH_{av} = 11.8 ± 0.5 kJ mol^{-1}; ΔS_{av} = 54 ± 3 J K^{-1} mol^{-1}) (Ag) and $T_c^{down} = 163$ and $T_c^{up} = 171$ K (ΔH_{av} = 4.9 ± 0.5 kJ mol^{-1}; ΔS_{av} = 30 ± 3 J K^{-1} mol^{-1}) (Au) (Fig. 26 right). The large difference in ΔS_{av} between silver and gold derivatives correlates with the difference of unit cell volume upon SCO ΔV = 49.71 and 33.21 Å^3 for the Ag and gold derivatives, respectively. Dehydration provokes dramatic changes in the SCO properties. Despite the fact that the two iron sites have an [FeN$_6$] core in the dehydrate forms, a 50% transition is still observed for the silver derivative but shifted ca 90 K to low temperatures and centered at 132.5 K with a 17 K wide hysteresis. The gold derivative is a HS CP after dehydration [25]. These results are consistent with those obtained for **MBrpmd** since the M = Au derivative is HS and a strongly cooperative half transition is observed for M = Ag at $T_c^{down} = 149$ and $T_c^{up} = 167$ K. The corresponding thermodynamic parameters referred only to the SCO centers are ΔH_{av} = 12 ± 0.5 kJ mol^{-1}; ΔS_{av} = 76 ± 3 J K^{-1} mol^{-1}) [26].

Both **MpmdH$_2$O** compounds have quite different thermal-induced SCO under pressure, despite their isostructural character (Fig. 27). Although the critical temperatures increase as pressure increases in both compounds, the silver derivative is more sensitive to pressure, i.e. a change of about 100 K is observed for the Ag derivative in the pressure interval 10^5 Pa–0.34 GPa [27], while only a shift of 20 K is observed for the Au compound in the same range of pressure. For **AgpmdH$_2$O**, the pressure dependence of the critical temperatures is sigmoidal indicating a cooperative behavior characterized by a piezo-hysteresis ca 0.1 GPa wide [27]. This is reflected in the increase of the thermal hysteresis and in the room-temperature shift of the thermo-hysteresis in the interval 0.2–0.4 GPa for **AgpmdH$_2$O** (Fig. 27 top). This strongly contrasts with **AupmdH$_2$O** in which a further increase of pressure does not involve neither an increase of T_cs nor cooperativity [28]. The coop-

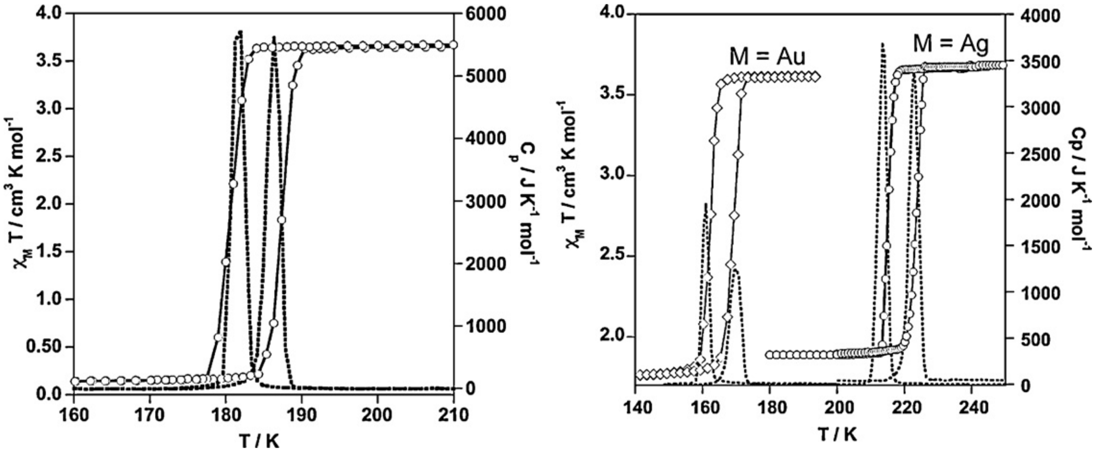

Fig. 26. Magnetic and calorimetric properties of **Agpmd$_2$**-β (left) and **MpmdH$_2$O** (M = Ag, Au) (χ_M = magnetic susceptibility, T = temperature, and C_p = anomalous molar heat capacity).

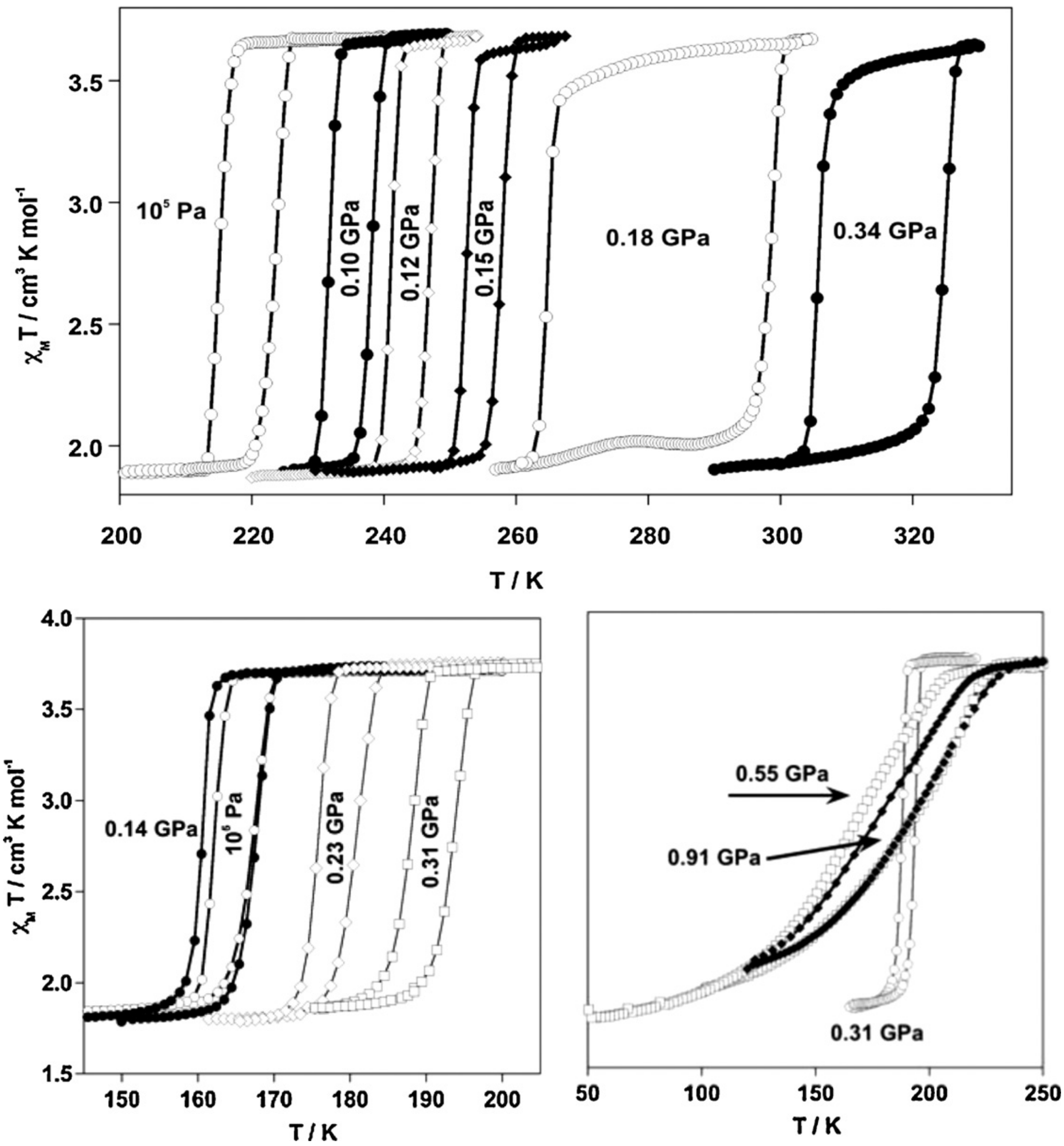

Fig. 27. Pressure dependence of the SCO behavior of **AgpmdH$_2$O** (top) and **AupmdH$_2$O** (bottom) (χ_M = magnetic susceptibility, T = temperature). Adapted from Ref. [27].

erative response of **AgpmdH$_2$O** to pressure has also been checked at 300 K using visible absorption spectroscopy. In these conditions a hysteresis of ca 0.2 GPa was observed (Fig. 28) [27].

3.3. *Bismonodentate pyridine-like ligands*

The utilization of the bis-monodentate ligands pyrazine (pz), 4,4′-bipyridine (4,4′-bipy) and bispyridylethene (bpe) has afforded a series double interpenetrated 3D networks of formula $\{Fe(L)_n[Ag(CN)_2]_2\}$ (n = 1 or 2 for L = pz or with L = 4,4′-bipy or bpe) [29]. In these compounds, the Fe(II) atom defines an elongated octahedron whose equatorial positions are occupied by the CN moieties of the $[Ag(CN)_2]^-$ anions. Each $[Ag(CN)_2]^-$ anion connects two Fe(II) atoms defining 2D $\{Fe_4[Ag(CN)_2]_4\}_\infty$ grids, which stack in such a way, that the Fe(II) atoms of a particular grid are above and below the centers of the windows defined by the adjacent grids. The axial positions of each iron atom are occupied by two organic bridging ligands L, which link another Fe(II) (pz) atom or a Ag(I) (4,4′-bipy and bpe) atom belonging to alternate $\{Fe_4[Ag(CN)_2]_4\}_\infty$ layers, so that each $\{Fe_4[Ag(CN)_2]_4\}$ window of

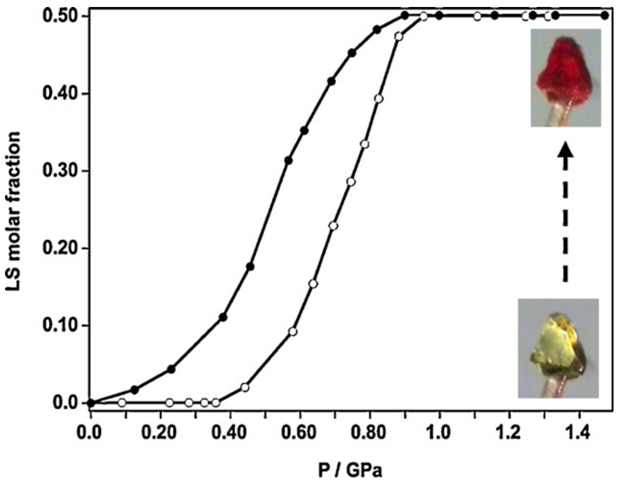

Fig. 28. Pressure dependence of the LS molar fraction deduced from visible spectra of **AgpmdH$_2$O** in the solid state.

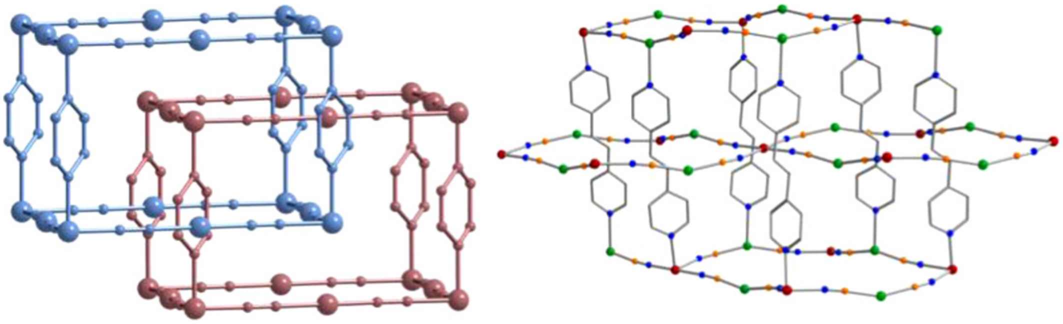

Fig. 29. Schematic view of two interpenetrated frameworks of $\{Fe(pz)[Ag(CN)_2]_2\}$ (left) and $\{Fe(bpe)_2[Ag(CN)_2]_2\}$ (right).

a contiguous layer is threaded by one (pz) or two (4,4′-bipy and bpe) organic bridges (Fig. 29). The pz derivative is diamagnetic and the 4,4′-bipy is paramagnetic in the whole range of temperature. Despite the structural similarities of the 4,4′-bipy and bpe derivatives (the average Fe–N bond length is 0.011(9) Å greater for the 4,4′-bipy derivative) the bpe derivative undergoes a very cooperative and singular spin transition at atmospheric pressure. Samples consisting of single crystals show one of the broadest thermal hysteresis loops observed for a SCO system, ca. 95 K wide, between 120 K and 215 K. However, this hysteresis disappears after annealing at the same time that the extent of the transition decreases and becomes 50%. The single crystals transform into a microcrystalline powder after five or more cycles. The spin state of both derivatives display strong pressure dependence. Around 85% of the spin change takes place within the range of 0.2 GPa at room temperature indicating that these 3D networks are extremely sensitive to pressure variations.

4. Tetracyanometallate complexes

Tetracyanometallate based SCO-CPs belong to the well-known series of Hofmann clathrates whose paradigm is the 2D CP $\{Ni(NH_3)_2[Ni(CN)_4]\}\cdot 2G$ (G = guest molecule) [30]. In these compounds the structural principles concerning the octahedral $[FeN_6]$ site remain unaltered with respect to those already discussed for the dicyanometallates. Obviously, the major structural differences stem from the change of connectivity/geometry and rigidity generated by the bridging square planar anion $[M(CN)_4]^{2-}$. Indeed, connectivity is twice that mediated by $[M(CN)_2]^-$ giving more dense and robust frameworks. This enables more effective transmission of the structural changes associated with the SCO and, hence, the occurrence of larger thermal hysteresis loops, which are synonymous with stronger cooperative behavior.

4.1. Two-dimensional pyridine based compounds

Self-assembly of Fe(II), monodentate ligands derived from pyridine and tetracyanometallate complexes $[M(CN)_4]^{2-}$ have provided a series of CPs formulated $\{Fe(L)_2[M(CN)_4]\}$ where M = Ni, Pd, Pt and L = py (**MHpy**) [31], (2,3,4)-Mepy (**MMepy**) [32], 3-Xpy (X = F, Cl, Br, I) (**M3Xpy**) [33], 4-phenylpyridine (4phpy) (**M4phpy**) [21,34] and 4-tetrathiafulvalenylcarboxamidopyridine (ttf-adpy) (**Mttf-adpy**) [35]. The ligand 5Brpmd acts as a monodentate ligand in presence of $[M(CN)_4]^{2-}$ to give $\{Fe(5Brpmd)_2[M(CN)_4]\}$ (**M5Brpmd**) [26]. Most of these compounds display interesting cooperative SCO properties.

4.1.1. Structure

The crystal structure of **NiHpy**, several members of the **M3Xpy** family and the **MMepy** series are known. **NiHpy**, **M3Fpy**, **M3Ipy** and **Pt3Clpy** are isostructural and crystallize in the monoclinic *C*2/*m* space group while the remaining **M3Clpy** (M = Ni, Pd) and **M3Brpy** display the orthorhombic Pnc2 space group at room temperature. However, **Pd3Clpy** changes to the *pmna* space group at 150 K when the system is just in the middle of the plateau of a two-step spin transition (ST) where 50% of HS and LS sites are present. X-ray powder diffraction data (XRPD) indicates that **Ni5Brpmd** is isostructural to the latter series. In contrast, the XRPD of **M5Brpmd** (M = Pd and Pt) suggest that both derivatives are isostructural with the monoclinic C2/m series. The **MMepy** series crystallize in the centrosymmetric orthorhombic Cmmm (2-Me, 3-Me) and monoclinic *C*2/*m* (4-Me) space groups.

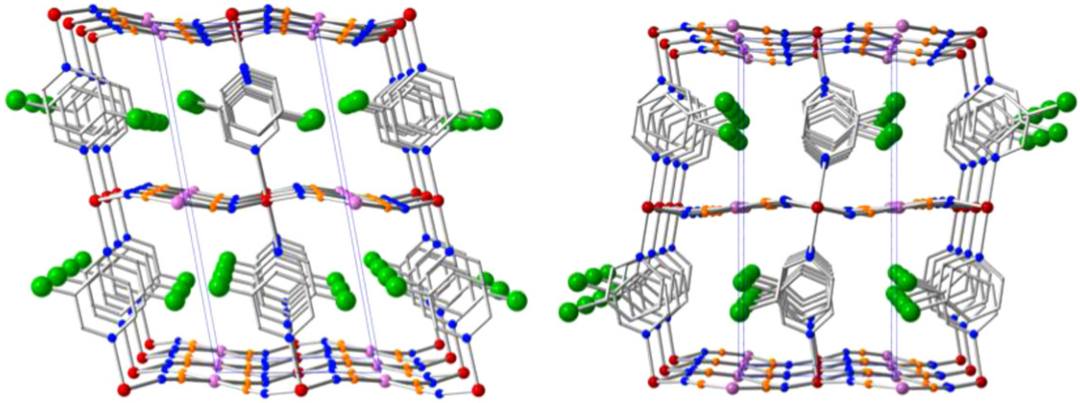

Fig. 30. Packing of three consecutive layers showing interdigitation of the 3-Xpy groups and distinct orientation of the halide X atom, monoclinic C2/m (left) and orthorhombic Pnc2. Color code: Fe (red), M (pink), N (blue), C (orange), and X = F, Cl, Br, I (green).

Table 1
Hofmann-like two-dimensional spin crossover coordination polymers (2D SCO-CPs).

Compound	SCO[a]	T_c^{up} (K)	T_c^{down} (K)	ΔT_c (K)	ΔH_{av} (kJ/mol)	ΔS_{av} (J/K mol)	Refs.
$Fe(py)_2[Ni(CN)_4]$	i	186	195	9	–	–	[31,36]
$Fe(py)_2[Pd(CN)_4]$	c	208	213	5	14.5	68	[36]
$Fe(py)_2[Pt(CN)_4]$	c	208	216	8	14.7	70	[36]
$Fe(3\text{-}Fpy)_2[Ni(CN)_4]$	c	205.8	234.4	28.6	19.1	87.4	[33]
$Fe(3\text{-}Fpy)_2[Pd(CN)_4]$	c	213.6	248.4	34.8	21.4	93.4	[33]
$Fe(3\text{-}Fpy)_2[Pt(CN)_4]$	c	214.0	239.5	25.5	20.6	91.7	[33]
$Fe(3\text{-}Clpy)_2[Ni(CN)_4]$	50%	105.8	123.4	17.6	–	–	[33]
$Fe(3\text{-}Clpy)_2[Pd(CN)_4]$	Two-step	(1) 169.6 (2) 141.4	(1) 164.5 (2) 148.4	(1) 4.9 (2) 7	(1) 8.8 (2) –	(1) 48.7 (2) –	[33]
$Fe(3\text{-}Clpy)_2[Pt(CN)_4]$	c	141.1	161.4	19.3	10.6	70.4	[33]
$Fe(5\text{-}Brpmd)_2[Ni(CN)_4]$	c	170	180	10	11	62	[26]
$Fe(5Brpmd)_2[Pd(CN)_4]$	c	204	214	10	16	76	[26]
$Fe(5\text{-}Brpmd)_2[Pt(CN)_4]$	c	197	223	26	16	81	[26]
$Fe(3\text{-}Mepy)_2[Ni(CN)_4]$	50%	87.5	105	ca 10	–	–	[38]
$Fe(4\text{-}phpy)_2[Ni(CN)_4]$	i	135	158	23	7.8[c]	55.7[c]	[21,34]
$Fe(4\text{-}phpy)_2[Pd(CN)_4]$	c	163	203	40	11.8	64.1	[21]
$Fe(4\text{-}phpy)_2[Pt(CN)_4]$	c	185	225	40	12.8	64	[21]
$Fe(ttfadpy)_2[Ni(CN)_4]$[b]	Two-step	(1) 172 (2) 111		–	–	–	[35]
$Fe(ttfadpy)_2[Pd(CN)_4]$[b]	Two-step	(1) 228 (2) 197		–	(1) 5.7 (2) 6.5	(1) 24 (2) 30.4	[35]
$Fe(ttfadpy)_2[Pt(CN)_4]$[b]	Two-step	(1) 228 (2) 202		–	(1) 6.2 (2) 7.2	(1) 26.6 (2) 32.8	[35]

[a] i: incomplete and c: complete.
[b] These compounds contain 1.5–2 molecules of H_2O.
[c] This compound displays ca 14.6% of HS impurities in the LS state. Extrapolation to 100% gives $\Delta H = 9.1\ kJ\ mol^{-1}$ and $\Delta S = 65\ J\ K^{-1}\ mol^{-1}$.

These compounds consist of pseudo-octahedral Fe(II) sites, the equatorial positions of which are interconnected through $[M(CN)_4]^{2-}$ bridging groups to afford 2D grids characterized by $\{Fe_2[M(CN)_4]_2\}$ square windows. Two layers are disposed in such a way that the Fe(II)/M(II) atoms of one particular layer are in the vertical of the barycenter of the $\{Fe_2[M(CN)_4]_2\}$ windows belonging to the layers immediately below and above. The crystal packing of both series differ somewhat due to the non-centrosymmetric nature of the orthorhombic series. These differences are evidenced in Fig. 30.

4.1.2. Spin crossover properties

The spin crossover properties deduced from magnetic and calorimetric measurements are summarized in Table 1 for the SCO members of these series of compounds. Except for the **Mttf-adpy** family [35], which undergo poor cooperative two-step ST, the remaining compounds display strong cooperative ST accompanied with large hysteretic behavior. This cooperativity is reflected in the large entropy variation (ΔS) observed for most of these compounds. In particular, the **M3Fpy** series exhibits the highest ΔS variations ever obtained from DSC measurements for an SCO compound. The ΔS values are close to $90\ J\ K^{-1}\ mol^{-1}$, approximately 10-30% greater than those reported for related 2D (**MHpy**, **M5Brpym**, **M4phpy**) and 3D ($\{Fe(pz)[M(CN)_4]\}$ [36], vide infra) compounds, respectively. ΔS has two components, one of electronic origin $\Delta S_{el} \approx 13.45\ J\ K^{-1}\ mol^{-1}$ and other of vibrational origin, ΔS_{vibr}. The later ($\Delta S_{vibr} = \Delta S - \Delta S_{el}$) contains information about cooperativity. An estimation of the ΔS_{vibr} value based on vibrational spectroscopy was performed for the **MHpy** and the $\{Fe(pz)[M(CN)_4]\}$ series based on vibrational spectroscopy [37]. Most low-frequency modes suffer dramatic changes upon spin transition. For example, the stretching modes of the $[FeN_6]$ core change by $160–180\ cm^{-1}$, a fact already noted for other Fe(II) SCO compounds. However, important and genuine additional sources of entropy are the stretching M–C and bending M–C–N modes of the $[M(CN)_4]^{2-}$ building block. These modes experience shifts of approximately $40–70\ cm^{-1}$ and $150\ cm^{-1}$, respectively, which indicate they are strongly coupled with those of the $[FeN_6]$ core. This is a reasonable observation because both building blocks, covalently bonded, afford a robust $\{Fe[M(CN)_4]\}_\infty$ 2D framework, which enables long-range elastic interactions responsible, in part, for the cooperativity and hysteresis exhibited for these compounds.

The axial ligand seems also to play a significant role in the transmission of cooperativity. For example, in the essentially isostructural **M3Hpy** and **M3Fpy** series, the pyridine rings of consecutive layers interdigitate defining infinite stacks characterized by an almost face-to-face superposition along the [0 1 0] direction (Fig. 30). The resulting weak π–π interactions (C···C distances of approximately 3.75–3.90 Å) couple the layers with similar efficiency. However, the cooperativity is significantly smaller for **M3Hpy**. The higher ΔS_{vibr} values found for the **M3Fpy** compounds are in line with the cooperative nature of their SCO behavior (larger hysteresis loops). It is not obvious to rationalize why substitution of a hydrogen atom by a fluorine atom in the 3-position provokes such a dramatic increase in cooperativity and the ΔS_{vibr} value. However, the weakly polarizable F atoms fill the channels ([010] direction) more efficiently than the H atoms; hence, it should be expected that the 3-Fpy ligands facilitate the propagation of certain vibrational modes better than py ligands. This conjecture is in line with the noticeable diminution of cooperativity observed when moving from the **M3Fpy** series to the **M3Clpy** series. Although larger than the F atom, the Cl atom is more polarizable and may act more efficiently as a "shock-absorber" than as a "shock-transmitter"; it thus minimizes the transmission of the structural changes/vibrational modes associated with SCO. However, as seen in Table 1 the **M4phpy** series evidences that the relationship between ΔS_{vibr} and wideness of hysteresis is not simple since the Pd and Pt derivatives show large hysteresis loops but comparatively small ΔS values. This could be related with the fact that the ST occurs concomitantly with a crystallographic phase transition in the latter compounds. Unfortunately, the crystal structure of this series is unknown.

Regardless M^{II} (Ni, Pd or Pt), the critical temperatures follow approximately the following trend:

$$3\text{-Mepy} \leq 3\text{-Clpy} \ll \text{ttf-adpy} \approx 4\text{-phpy} \approx 5\text{-Brpmd} \leq \text{Hpy} < 3\text{-Fpy}$$

Table 2 summarizes differences of the average critical temperatures, ΔT_c^{av}, between **M3Fpy** (M = Ni, Pd, Pt) and the corresponding

Table 2
Difference of the average critical temperature, ΔT_c^{av}, between M3Fpy and the corresponding CPs of the other series.

ΔT_c^{av} (**M3Fpy-ML**)/K	L					
	3-Mepy	3-Clpy	4-phpy	ttf-adpy	5-Brpmd	Hpy
Ni	124	105	73	78	45	30
Pd	–	78	48	18	22	20
Pt	–	5	22	12	17	15

members of the other series. The general trend is a marked destabilization of the LS state when moving from Hpy to 3-Mepy and from Pt to Ni derivatives. On one hand, the dependence of T_c^{av} on the nature of the axial ligand should be understood, as discussed for $[M(CN)_2]^-$ (M = Ag, Au) derivatives, in terms of how chemical pressure influences the effective ligand field strength felt by the iron(II). On the other hand, the influence of the metal M on T_c^{av} is much more mitigated than observed for Ag, Au couple, in fact the differences are in general insignificant. However, more significant differences are observed when comparing with Ni, for example ΔT_c^{av} (**Pd3Clpy-Ni3Clpy**) = 38 K, ΔT_c^{av} (**Pt3Clpy-Ni3Clpy**) = 37 K.

Ni3Mepy and **Ni3Clpy** are surprisingly similar since they have comparable structures, undergo 50% cooperative ST characterized by the lowest critical temperatures in the series and, furthermore, they display similar pressure dependence of the SCO affording two-step ST in the pressure interval 0.3–0.4 GPa (Fig. 31a). The two-step ST observed for **Ni3Clpy** is consistent with that observed for its isostructural Pd counterpart (Fig. 31c). The crystal structure data of the latter, obtained in the middle of the plateau where 50% of spin conversion occurs, reveal that a “re-entrant” crystallographic phase transition accompanies this transition [33,38].

The influence of pressure on the thermally induced ST of **M3Fpy** shows that the hysteresis loop essentially keeps its original square shape, as observed for **AgpmdH$_2$O** (see Fig. 26), which indicates that the cooperativity is not affected by pressure in the range of pressures measured (Fig. 31b). Furthermore, it is possible to control the critical temperatures of the transition and pushing them upward so that the hysteresis loop includes room temperature. This is a remarkable result because room-temperature switches and memories are of singular relevance in the science of materials,

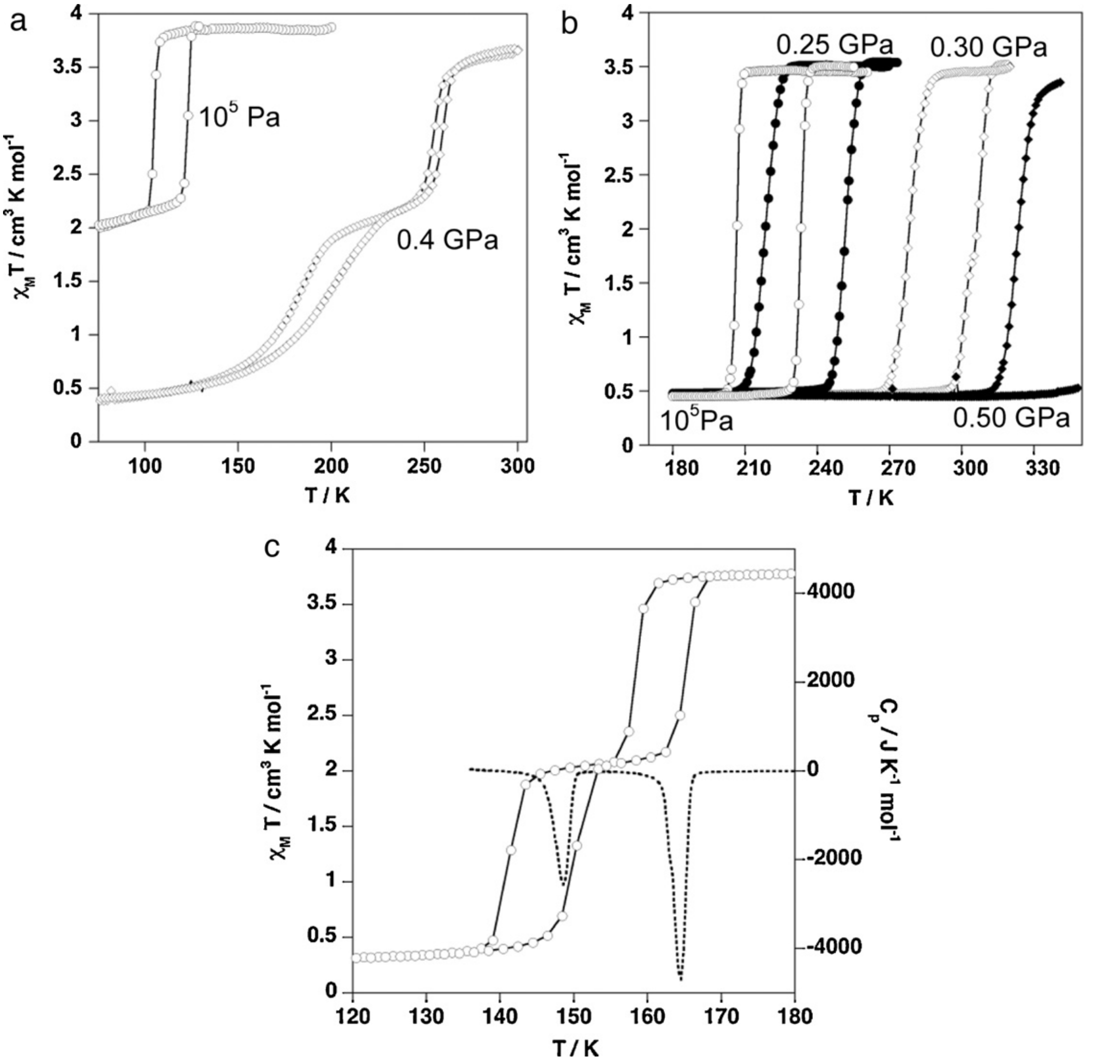

Fig. 31. Pressure dependence of the SCO behavior of **Ni3Clpy** (top left) and **Ni3Fpy** (top right). Magnetic and calorimetric properties of **Pd3Clpy** (bottom) (χ_M = magnetic susceptibility, T = temperature, and C_p = anomalous molar heat capacity).

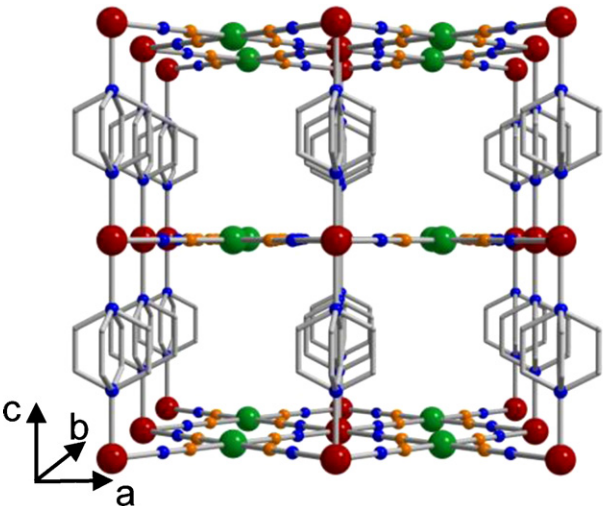

Fig. 32. View of a fragment of the 3D porous SCO-CPs **Mpz** (M = Ni, Pd, Pt) (the water molecules are not shown). Color code: Fe (red), M (green), N (blue), and C (orange).

particularly if these properties are combined with drastic changes of color as observed for the **M3Fpy** series.

4.2. Three-dimensional bismonodentate pyridine-like based compounds

Formal substitution of the pyridine by pyrazine (pz) or 4,4′-azopyridine (azpy) in **MHpy** (M = Ni, Pd, Pt) has afforded the first 3D SCO frameworks {Fe(L)[M(CN)$_4$]}·nH$_2$O (L = pz (n = 2), **Mpz** [36]; L = azpy (n = 1), **Mazpy** [39]) able to function as true Hofmann-like clathrates due to their porous nature.

The very first motivation in undertaking the study of **Mpz** was to explore the influence of dimensionality on cooperativity by comparing two closely related SCO-CPs. The three isostructural derivatives, M = Ni, Pd and Pt, crystallize in the tetragonal *P*4/*mmm* space group. Like in the pyridine derivative, the Fe(II) cations and the [M(CN)$_4$]$^{2-}$ anions assemble to give parallel {Fe[M(CN)$_4$]}$_\infty$ layers, which stack along [0 0 1] direction. The pyrazine ligands bridge the iron atoms of adjacent layers defining a 3D porous network characterized by square channels running along [1 0 0] and [0 1 0] directions where typically two molecules of water are located (Fig. 32). **Mazpy** series have the same structure as **Mpz** except for the azpy pillars, which separates the {Fe[M(CN)$_4$]}$_\infty$ layers by ca 13.5 Å. Consequently, the accessible volume changes from ca. 131 Å^3 for **Ptpz** to ca. 286 Å^3 for **Ptazpy**. Despite this, only one solvent molecule per formula occupies the pores of the latter.

The **Mpz** series display magnetic, chromatic and structural bistability at room temperature characterized by a hysteresis loop ca 25 K wide where the two different spin states coexist and can be easily detected. However, noticeable variability of the critical temperatures and shape of the thermal induced SCO was found at the first stages of the characterization of these materials (Fig. 33 left). Most probably, the high insolubility and the porous nature of these compounds connected with the formation of defects, different solvates and/or polymorphs are at the heart of the observed differences. Anyway, reliable square-shaped hysteresis loops are obtained in the temperature interval 280–310 K for **Mpz** after treating the sample at ca 400 K for 1 h (Fig. 33 left) [40]. The dramatic influence of the number of water molecules on the SCO of the **Ptpz** derivative is illustrated in (Fig. 33 right). The presence of n = 0–2 H$_2$O molecules has no apparent effect on the SCO. In contrast, the SCO becomes incomplete and the critical temperatures decrease for larger H$_2$O content; finally for n = 5 the system is paramagnetic in the whole range of temperatures [28].

Clearly, the 3D **Mpz** frameworks undergo stronger cooperative ST with higher T_c values and larger hysteresis loops than the **MHpy** pyridine counterparts (see Table 1). These significant differences in T_c cannot be explained in terms of the spectrochemical series since pyridine imparts stronger ligand field than pyrazine. Thus, the chemical pressure originating in the more rigid **Mpz** structures may be responsible for the effective stronger ligand field at the iron(II) site. The observed broader hysteresis loops and higher critical temperatures can be considered two consequences of the difference in the dimensionality in two closely related structures.

Isomorphic substitution of iron(II) by nickel(II) and cobalt(II) in the solid solutions {Fe$_{1-x}$M$_x$(pyrazine)[Pt(CN)$_4$]} (M = Ni(II) or Co(II)) has afforded interesting information concerning the cooperative nature of the ST in the **Mpz** series. The isomorphic substitution (increasing x) “switches off” the communication between the iron centers (cooperativity) and, hence tends to smooth the ST, decrease the critical temperatures and narrow the hysteresis loop, which vanishes for $x \approx 0.5$ (Fig. 34). Similarly, ΔS (and ΔH) linearly decreases as x increases. This observation correlates quite well with the linear dependence on x found for two relevant low frequency Raman vibrational modes associated to the LS and HS states in the 50–150 cm^{-1} range. These results demonstrated for the first time

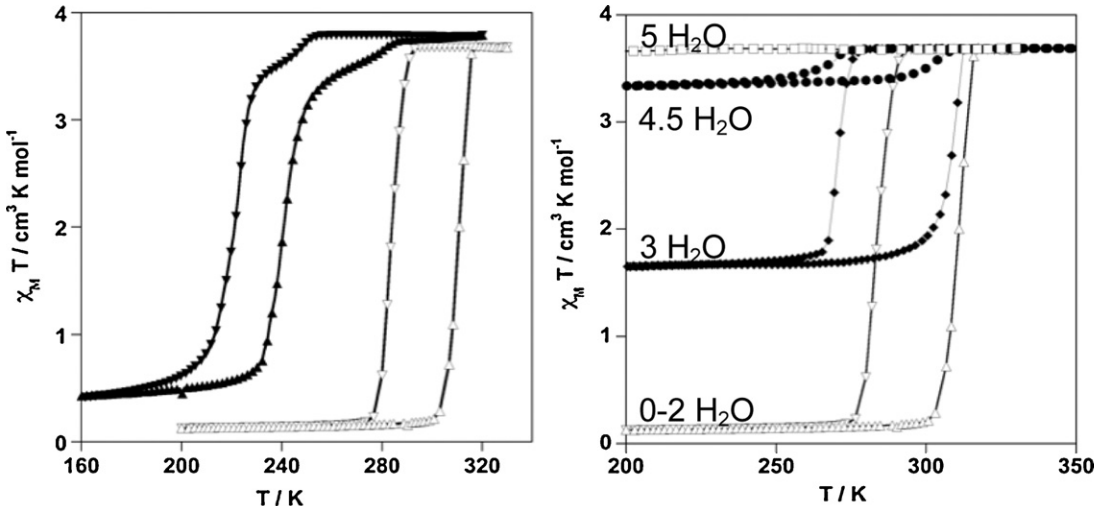

Fig. 33. (Left) Magnetic properties of Ptpz originally reported in [36] (closed triangles) and after thermal treatment at ca. 400 K for 1 h (open triangles). (Right) Influence of the molecules of water of the SCO of **Mpz** (M = Pt in this particular case) (χ_M = magnetic susceptibility, T = temperature).

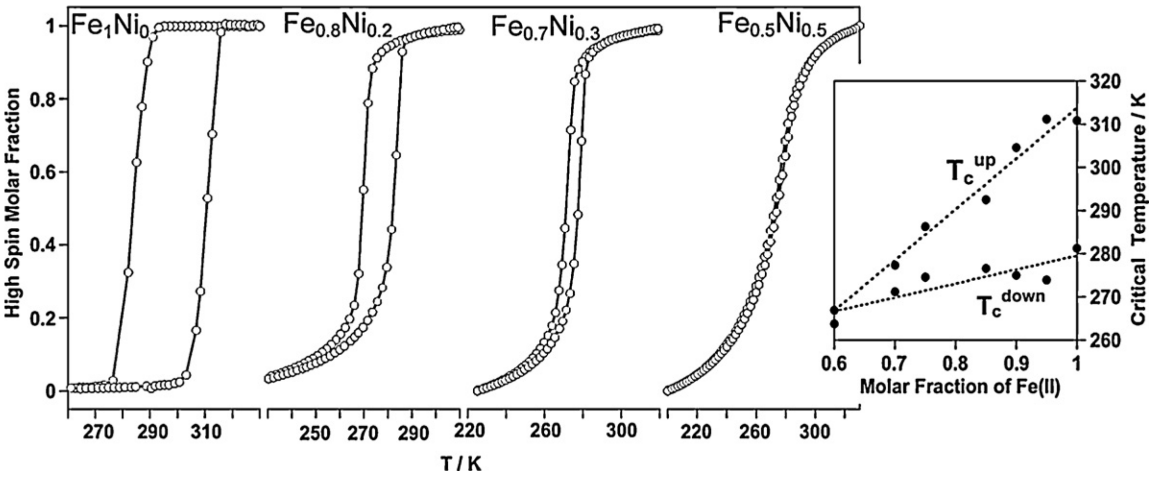

Fig. 34. SCO behavior of the isomorphic solid solutions $\{Fe_{1-x}Ni_x(pyrazine)[Pt(CN)_4]\}$. Inset: evolution of the critical temperatures as a function of x.

that there is a correlation between vibrational frequencies and the entropy variation, which drive the cooperative nature of the SCO phenomenon [40].

An important consequence of the strong cooperative behavior observed for **Mpz** is the occurrence of bi-directional photo-induced structural phase transformation accompanied by switch between the HS and LS states when irradiating, inside the hysteresis region, with a nano-second pulsed laser ($\lambda = 532$ nm) on bulk and single-crystal samples [41]. Since this transition occurs around room temperature over a wide range of bistability and involves magnetization and color changes as well, it opens up interesting perspectives for applications in memory devices and optical switches. Furthermore, this observation is a good platform to investigate the interplay between light and cooperative electron-lattice interactions.

Compared with the **Mpz** series, the monohydrate **Mazpy** derivatives show much less cooperative SCO behavior with average critical temperatures, T_c^{av}, centered at 245 K (**Niazpy**), 291 K (**Pdazpy**) and 280 K (**Ptazpy**). The two latter transitions are characterized by a hysteresis loop 9 K and 10 K wide, respectively. Although the molecule of H_2O included in the channels does not interact appreciably with the framework, T_c^{av} is shifted ca 100 K to low temperatures upon dehydration (191 K for **Pdazpy** and 182 for **Ptazpy)** with concomitant increase of the hysteresis loop to ca 20 K. It is worth noting that, despite the hysteretic behavior, the transitions are quite smooth for the precipitated samples most probably due to the high insolubility of these compounds, which induce crystallite size inhomogeneity and consequently a wide distribution of critical temperatures. This seems evident when comparing the magnetic behavior of precipitated and single crystals of **Ptazpy** (Fig. 35). The latter show discontinuous transitions and well-defined T_c's [42].

Like for the 2D **M4phpy** derivatives, the relatively low T_c temperatures observed for the **Ptazpy** compounds allow to observe light-induced spin state trapping phenomenon (LIESST effect) at temperatures below 100 K.

5. Hexa- and octacyanato complexes

Hexa- and octa-cyanometallate building blocks have been extensively used for the construction of CPs exhibiting magnetic ordering. A relatively small fraction of these undergo thermal- pressure- and light-induced valence tautomeric phenomena, namely spin state change associated with metal-to-metal electron transfer process [43]. However, as far as we know only two examples are reported to undergo a pure SCO phenomenon.

The Prussian-blue analogue $\{CsFe[Cr(CN)_6]\}$ crystallizes in the cubic F-43m space group. The $[Cr(CN)_6]^{3-}$ building blocks connect six iron(II) atoms which are coordinated by six $[Cr(CN)_6]^{3-}$ ligands (Fig. 36 left). This compound undergoes a cooperative ST characterized by $T_c^{down} = 211$ K and $T_c^{up} = 238$ K and a hysteresis loop $\Delta T = 27$ K wide. The high temperature phase (HT) contains 6% of LS Fe(II) centers while the low temperature phase contains 11% of Fe(II) ions in the HS state. Due to these HS impurities the solid shows spontaneous magnetization with magnetic ordering at 9 K [44]. In a subsequent study it was found that this compound displays an abrupt isosymmetric phase transition, accompanied by dramatic unit cell volume collapse, in the ascending branch of the ST, namely in the range 245–265 K (note that for the new sample the hysteresis loop was $\Delta T = 37$ K wide, $T_c^{down} = 208$ K and $T_c^{up} = 245$ K). This phase transition, accompanied by sudden transformation of the HS Fe(II) ions to the LS state, is induced by absorption of X-ray photons which generates photo-excited LS iron(II) domains whose size rapidly grows with time until the percolation threshold is reached and the structure collapse is triggered [45].

The octacyano-bridged Nb–Fe(II) bimetallic assembly $\{Fe_2[Nb(CN)_8](3\text{-}CH_2OHpy)_8\}$ $6H_2O$, where 3-CH_2OHpy is 3-

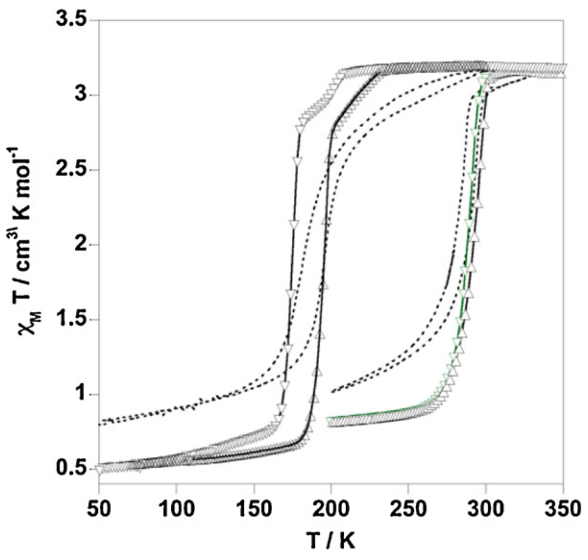

Fig. 35. Magnetic properties of samples constituted of single crystals (open triangles-solid line) and precipitated microcrystalline powders (dotted lines) for **Ptazpy** (χ_M = magnetic susceptibility, T = temperature).

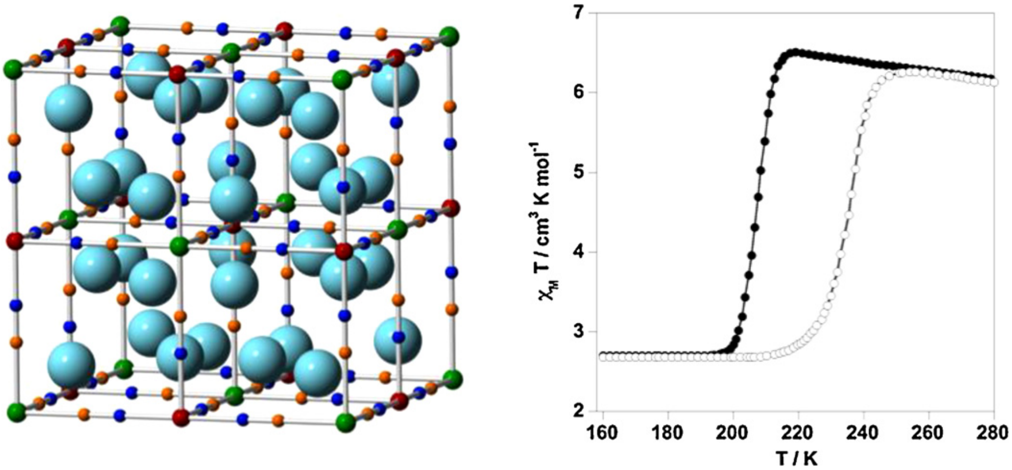

Fig. 36. Structure and magnetic properties of {CsFe[Cr(CN)$_6$]} [44,45]. Color code: Fe (red), Cr (green), N (blue), C (orange), Cs (blue). χ_M = magnetic susceptibility, T = temperature.

methanolpyridyl, crystallizes in the cubic *I*a-3*d* space group. The two axial positions of the Fe(II) ion are occupied by cyanide nitrogen atoms of $[Nb(CN)_8]^{4-}$ whereas the equatorial positions are occupied by four nitrogen atoms from (3-pyridyl)methanol ligands. The four equatorial CN groups of $[Nb(CN)_8]^{4-}$ bridge four Fe centers while the four axial CN groups are free (Fig. 37). This CP undergoes a continuous poorly cooperative SCO in the temperature range 350–150 K. Like in the precedent example, spontaneous magnetization (T_c = 12 K) reveals antiferromagnetic interactions between the residual HS iron(II) ions and Nb(IV) (S = 1/2) [46].

6. Physi- and chemo-sorption in iron(II) Hofmann-like SCO-CPs

The tetracyano bridged M-Fe(II) SCO-CPs **Mpz** are robust 3D frameworks with large empty channels. In addition to porosity, **Mpz** SCO-PCs feature first-order spin transition at room temperature and strong cooperativity characterized by a hysteresis loop 25 K wide. These attributes have enable to investigate synergies between host-guest chemistry and SCO phenomena in the room temperature bistability region, a quite unique example in molecular magnetism.

The guest-free **Mpz** (M = Ni [47,48], Pd and Pt [47]) framework adsorbs various guest molecules in the gas phase or solution and forms their clathrates. A bimodal reversible change of spin state at the iron(II) sites is observed concomitantly with the uptake of guest molecules. The HS clathrate, characterized by a yellow color, is stabilized by hydroxylic solvents, five- and six-membered aromatic molecules, while the LS clathrate, characterized by a red color, is stabilized by CS_2 [47] and CH_3CN [48] at 298 K. Smaller molecules like N_2, O_2 and CO_2 are retained in the framework without any effect in the spin state. For example, in the LS state at 298 K **Mpz** adsorbs benzene or pyrazine when exposed to vapors with simultaneous change of color from red to yellow while at same temperature in the HS state **Mpz** adsorbs CS_2 with simultaneous change to the red color characteristic of the LS state (Fig. 38 left). Pyrazine and benzene clathrates are paramagnetic in the whole

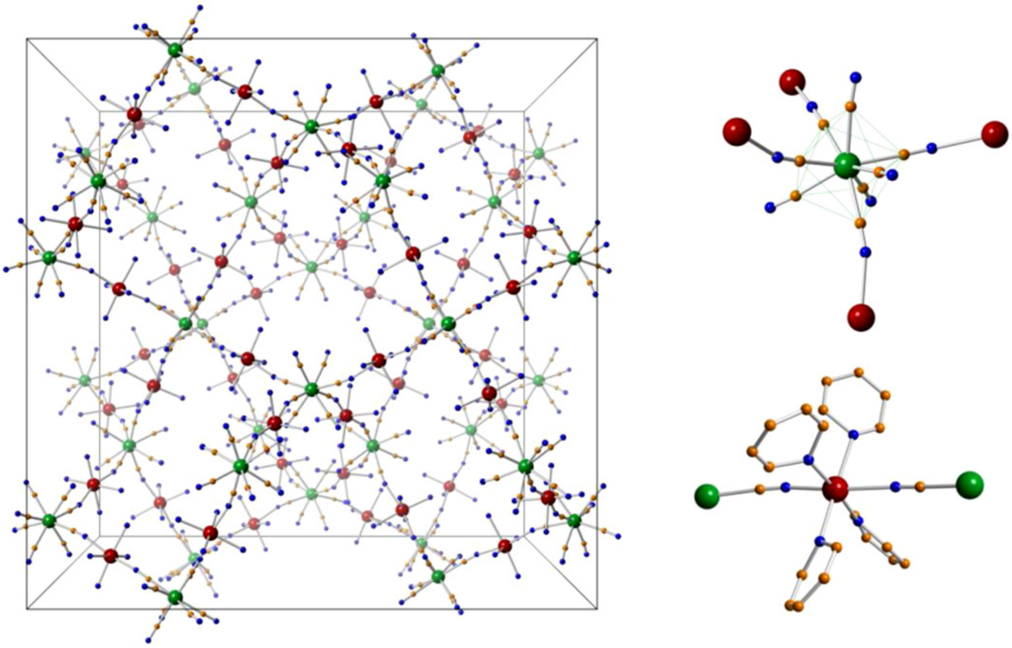

Fig. 37. Structure of {$Fe_2[Nb(CN)_8](3\text{-}CH_2OHpy)_8$} $6H_2O$ displaying the coordination surroundings and connectivity of Nb and Fe. Color code: Fe (red), Nb (green), N (blue), and C (orange).

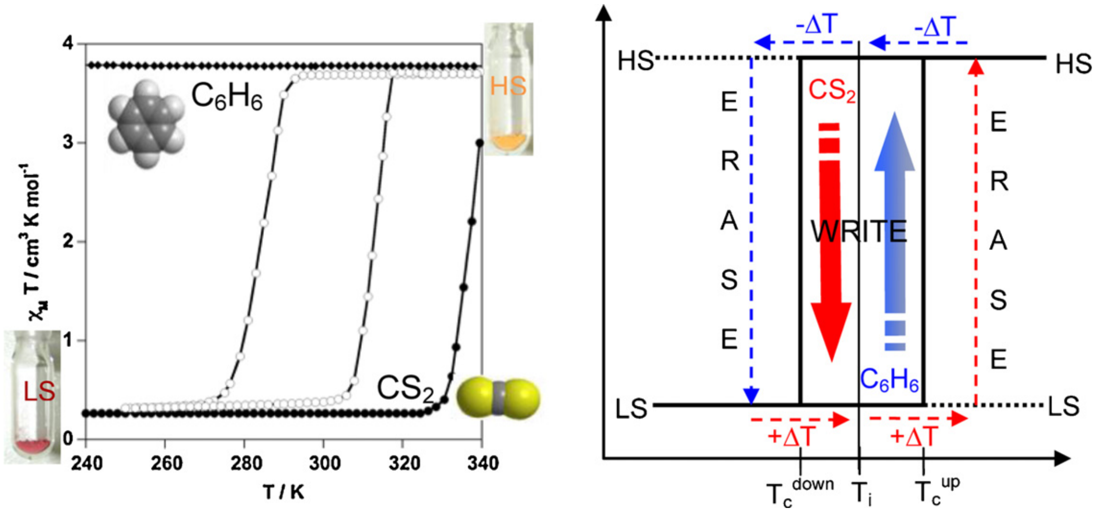

Fig. 38. (Left) Magnetic properties of the pristine **Ptpz** compound (open circles) and the corresponding C_6H_6 (diamonds) and CS_2 (closed circles) clathrates (χ_M = magnetic susceptibility, T = temperature). (Right) Scheme of the memory effect inside the hysteresis loop.

range of temperatures in contrast to the CS_2 clathrate, which is diamagnetic at temperatures below 330 K. Above this temperature the CS_2 molecule is desorbed with concomitant change to the HS state. Dynamic magnetic measurements have demonstrated that these sensory sorption–desorption processes take place very fast (within 2 min) [47]. Furthermore, they take place with memory since, for example, the system retains the HS state after desorption of benzene (WRITE). To recover the initial point (T_i) it is necessary to apply the operator $-\Delta T$+ΔT (ERASE). The opposite is true for CS_2 (Fig. 38 right).

Interestingly, the occurrence of coordinatively unsaturated Pt(II) centers enhances adsorptive selectivity for particular guests in **Ptpz**. In this respect, chemisorptive uptake of dihalogen molecules involving associative oxidation of Pt(II) to Pt(IV) and reduction of the dihalogen to the corresponding halide affords {Fe(pyrazine)[Pt(CN)$_4$(X)]} [X = Cl$^-$, Br$^-$, I$^-$]. According to Pt-4f-XPS experiments 50% of Pt(II) is oxidized to Pt(IV) despite all platinum atoms are crystallographically equivalent. The Pt(IV) sites are elongated octahedra with two X$^-$ anions in the axial positions while Pt(II) sites remain square planar (Fig. 39 left). The three derivatives undergo cooperative ST with critical temperatures T_c^{up} = 270 K (Cl), 324 K (Br) and 392 K (I) and T_c^{down} = 258 K (Cl), 293 K (Br) and 372 K (I). The trend shown by the T_c values reveals the sensitivity of the iron(II) coordination core to the "availability" of the lone electron pair cloud of the nitrogen atom in the Fe–NC–Pt–X moiety. The σ-donor capability of the nitrogen atom decreases as the electronegativity of X$^-$ increases, thereby inducing a decrease of the ligand field and the value of T_c. This conjecture is supported by the downward shift of the Pt(IV)-4f-XPS binding energy doublet when moving from 2Cl to 2I [49].

7. Processability at nanoscale level

Stepwise layer-by-layer epitaxial growth of Hofmann CPs through coordination reactions on gold surfaces was successfully applied fifteen years ago to fabricate thin films of the complex {Fe(4,4′-bipyridine)[Pt(CN)$_4$]} [50]. Based on this methodology, and using a combined top-down/bottom-up approach micro- and nano-sized patterns constituted of square motives of **Ptpz** were grown on gold surfaces [51,52]. Raman spectroscopy has been used to check the composition and structure of the motives as

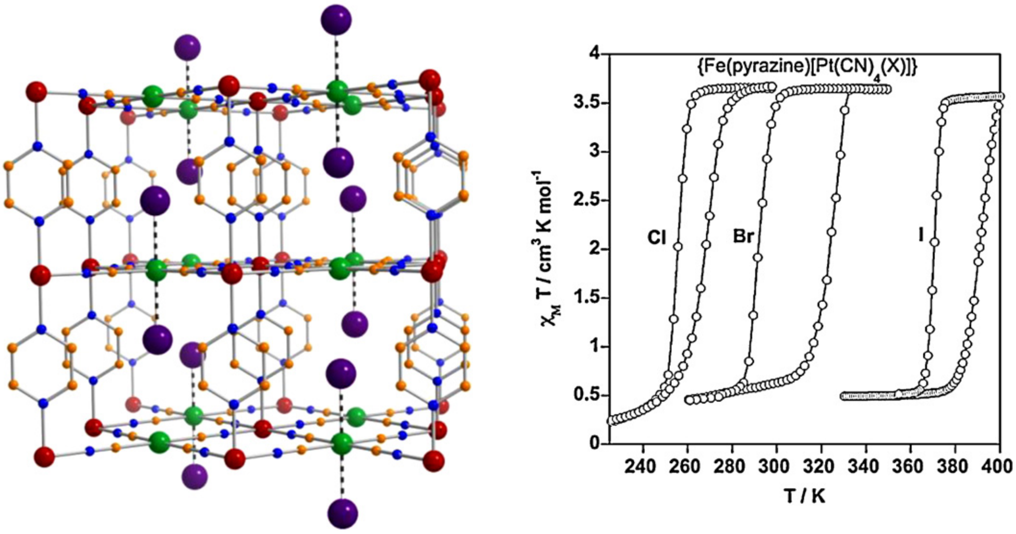

Fig. 39. Fragment of the structure showing a possible distribution for Pt(II) and Pt(IV) sites according to Pt-4f-XPS experiments (left) and magnetic properties (right) for {Fe(pyrazine)[Pt(CN)$_4$(X)]} [49].Color code: Fe (red), M (green), N (blue), C (orange), and X (violet). χ_M = magnetic susceptibility, T = temperature.

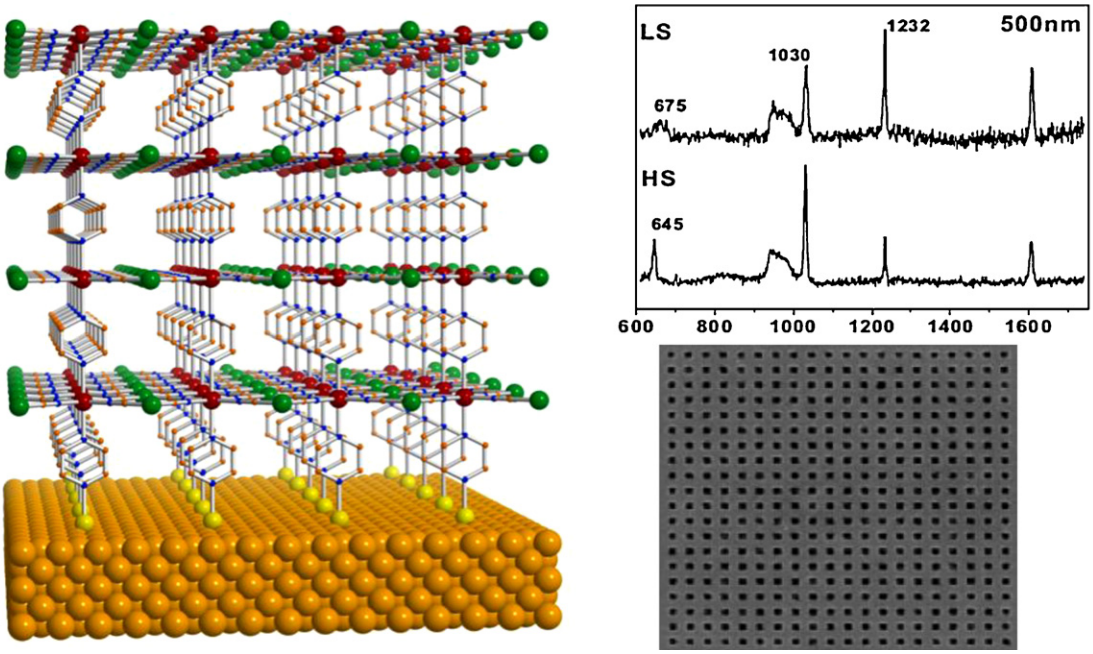

Fig. 40. (Left) Schematic representation of the ideal epitaxial growth of **Ptpz** on a 4-mercaptopyridine functionalized thin layer of Au. (Right) Nanopatterned thin film with 500 nm square motives of **Ptpz** (bottom) and the corresponding Raman spectrum for the HS and LS states (top) [53a]. Color code: Fe (red), Pt (green), N (blue), C (orange), S (light yellow), Au (dark yellow).

well as to probe the spin state. Assembled continuous and micropatterned (size ≥ 2 μm) thin films ca. 150 nm thick display similar SCO properties like the bulk material [51]. At smaller pattern sizes, the quantity of matter probed by the laser beam decreases significantly and, to record convenient spectra, the excitation power and time must be increased considerably. This leads, in turn, to laser heating of the sample to some extent and the pure LS spectrum is thus difficult to obtain. Nevertheless, Raman spectra of a single 500 nm object has been recorded and proved the occurrence of spin-state change (Fig. 40) [52]. Similar results have been obtained for the related **Mazpy** (M = Ni, Pd, Pt) Hofmann SCO-CPs [39].

An alternative and complementary approach to learn about the SCO phenomenon at nanometric scale is the synthesis of nanocrystals and nanoparticles. Water-in-oil micro-emulsion technique has afforded surfactant-free square shaped nanocrystals of **Ptpz** (Fig. 41, right) [53], which emulate the aforementioned square dots generated as nano-patterned thin films. From Table 3 and Fig. 41 left, three main consequences appear when the size of guest-free crystals decreases from the micrometer to the nanometer size: (i) increase of the residual HS fraction at low temperatures; (ii) decrease of the critical temperatures; and (iii) decrease of the hysteresis width. Apparently, these consequences seem to be closely related to the substantial increase of the specific surface area when

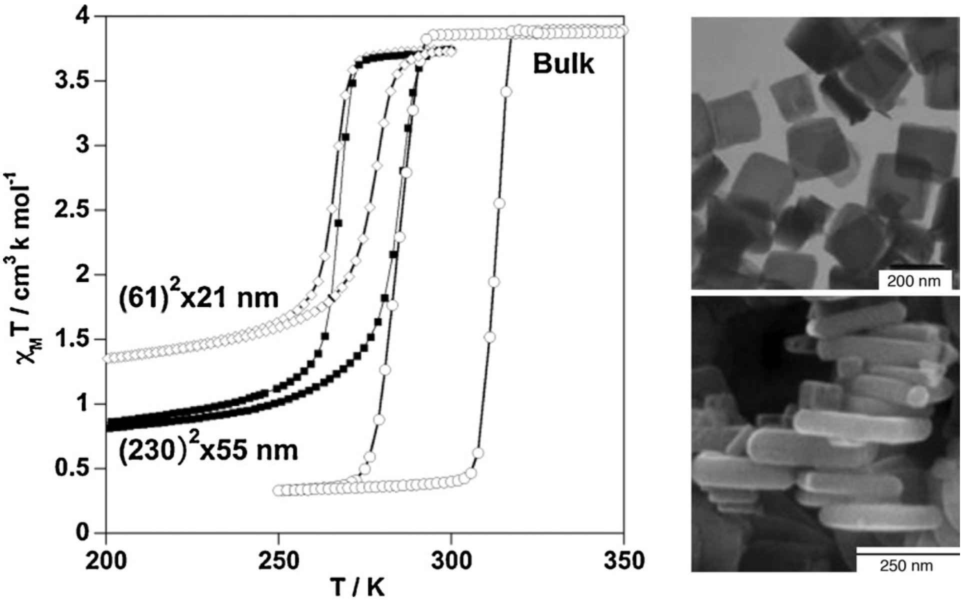

Fig. 41. (Left) Dependence of the magnetic properties on the crystal size (bulk, 230 nm × 230 nm × 55 nm, and 61 nm × 61 nm × 21 nm) of **Ptpz** (χ_M = magnetic susceptibility, T = temperature). (Right) TEM (top) and SEM (bottom) images of nanocrystals of **Ptpz**.
Adapted from Ref. [54].

Table 3
Size of the crystallites and the corresponding critical temperatures (K) and high-spin molar fraction (γ_{HS}) measured in the low temperature region were no SCO occurs.

Size	T_c^{down}	T_c^{up}	T_c^{av}	ΔT_c	γ_{HS}
Bulk ($s \leq 500\,\mu$m)	285	309	297	25	0
230 nm × 230 nm × 55 nm	266	288	277	22	14
61 nm × 61 nm × 21 nm	265	275	270	10	28
14.7 nm × 14.7 nm × 5 nm	262	268	265	6	34
7.7 nm × 7.7 nm × 3 nm	∼240	∼240	∼240	∼0	48

decreasing the size of nanocrystals. Residual paramagnetic impurities could be generated at the edge of the nanocrystals due to coordinative defects. This in turn will decrease the chemical pressure on the iron(II) SCO centers nearby the HS Fe(II) impurities (defects) thereby reducing T_c as well as cooperativity. Indeed, these effects are reminiscent of the properties described for the isomorphic solid solutions where dilution of the SCO centers reduces the size of the domains and consequently of the hysteresis. Similar conclusions have been obtained more recently for nanocrystals and poly(vinylpyrrolidone)-coated nanoparticles of the 2D SCO-Cps $\{Fe(3Fpy)_2[M(CN)_4]\}$ (M = Ni, Pd, Pt) (**M3Fpy**) [54]. From this study a clear logarithmic dependence of the average critical temperature versus size of nanoparticles has been observed. This functional form was previously reported for several physical properties in nanocrystals of different materials [55].

Ultra-small nanoparticles (3.8 nm) of **Nipz** have been grown using porous chitosan beads as matrix. In strong contrast with the results discussed above, these nanoparticles display cooperative ST with a hysteresis loop 10 K wide ($T_c^{down} = 208$ K and $T_c^{up} = 290$ K) despite only 33% of iron(II) ions undergo SCO [56]. This interesting observation is currently under investigation.

8. Conclusion

In summary, the last decade has witnessed the genesis of a new class of SCO coordination polymer (CPs) based on metallocyanate bridging ligands. Currently, more than 50 of such SCO-CPs are known and have contributed to the discovery of new important aspects of the SCO phenomenon. These new materials feature structural diversity, supramolecular isomerism, interpenetrating frameworks, structure flexibility, reversible solid-state chemical reactions, metallophilic interactions, porosity, physi- and chemisorption, or processability at nanoscale level, in addition to inherent SCO properties.

In particular, tetracyanometallate bridging ligands are excellent media to cooperatively propagate the SCO thus generating bistable materials. Some 2D SCO-CPs are quite sensitive to pressure, while keeping cooperativity, enabling fine-tuning of the critical temperature. Porous three-dimensional CPs based on the pyrazine ligand have afforded the best examples of bidirectional chemo-switching of spin state and memory effect at room temperature, which will open a route for evolving the porous CPs to environmentally responsive materials. These CPs are also excellent platforms to investigate cooperativeness at micro and nano-scale a fact which confers great potential for practical applications as eventually they could be integrated as memories and sensors in nano-sized optical and electronic devices.

Acknowledgements

This work was supported by the Spanish Ministerio de Ciencia e Innovación (MICINN) and FEDER funds (CTQ2010-18414) and the Generalitat Valenciana (GVACOMP2010-139).

References

[1] see for example;
(a) H.A. Goodwin, Coord. Chem Rev. 18 (1976) 293;
(b) P. Gütlich, Struct. Bonding (Berlin) 44 (1981) 83;
(c) E. König, G. Ritter, S.K. Kulshreshtha, Chem. Rev. 85 (1985) 219;
(d) A. Hauser, Comments Inorg. Chem. 17 (1995) 17;
(e) E. König, Struct. Bonding (Berlin) 76 (1991) 51;
(f) P. Gütlich, A. Hauser, H. Spiering, Angew. Chem. Int. Ed. Eng. 33 (1994) 2024;
(g) O. Sato, Acc Chem. Res. 36 (2003) 692;
(h) A. Bousseksou, G. Molnár, G. Matouzenko, Eur. J. Inorg. Chem. (2004) 4353;
(i) J.A. Real, A.B. Gaspar, V. Niel, M.C. Muñoz, Coord. Chem Rev. 236 (2003) 121;
(j) P. Gütlich, H.A. Goodwin (Eds.), Topics in Current Chemistry, vols. 233–235, 2004;
(k) J.A. Real, A.B. Gaspar, M.C. Muñoz, Dalton Trans. (2005) 2062;
(l) A.B. Gaspar, V. Ksenofontov, M. Seredyuk, P. Gütlich, Coord. Chem. Rev. 249 (2005) 2661;
(m) J.F. Létard, J. Mater. Chem. 16 (2006) 2550;
(n) M.A. Halcrow, Polyhedron 26 (2007) 3523.
[2] O. Kahn, J.P. Launay, Chemtronics 3 (1988) 140.
[3] See for example;
(a) J.F. Létard, P. Guionneau, E. Codjovi, O. Lavastre, G. Bravic, D. Chasseau, O. Kahn, J. Am. Chem. Soc. 119 (1997) 10861;
(b) B. Weber, W. Bauer, J. Obel, Angew. Chem. Int. Ed. 47 (2008) 1.
[4] (a) J.G. Haasnoot, G. Vos, W.L. Groeneveld, Z. Naturforsch., Teil B 32 (1977) 1421;
(b) A. Michalowicz, J. Moscovici, B. Ducourant, D. Craco, O. Kahn, Chem. Mater. 7 (1995) 1833.
[5] W. Vreugdenhil, J.H. van Diemen, R.A.G. de Graaff, J.G. Haasnoot, J. Reedijk, A.M. van der Kraan, O. Kahn, J. Zarembowitch, Polyhedron 9 (1990) 2971.
[6] J.A. Real, E. Andrés, M.C. Muñoz, M. Julve, T. Granier, A. Bousseksou, F. Varret, Science 268 (1995) 265.
[7] G.J. Halder, C.J. Kepert, B. Moubaraki, K.S. Murray, J.D. Cashion, Science 298 (2002) 1762.
[8] A. Galet, M.C. Muñoz, J.A. Real, Inorg. Chem. 45 (2006) 4583.
[9] G. Agustí, M.C. Muñoz, A.B. Gaspar, J.A. Real, Inorg. Chem. 48 (2009) 3371.
[10] (a) V. Niel, A.B. Gaspar, M.C. Muñoz, J.A. Real, Chem. Commun. (2003) 1248;
(b) G. Agustí, A.L. Thompson, A.B. Gaspar, M.C. Muñoz, A.E. Goeta, J.A. Rodriguez-Velamazán, M. Castro, R. Burriel, J.A. Real, Dalton Trans. (2008) 642.
[11] (a) M.C. Muñoz, A.B. Gaspar, A. Galet, J.A. Real, Inorg. Chem. 46 (2007) 8182;
(b) G. Agustí, M.C. Muñoz, A.B. Gaspar, J.A. Real, Inorg. Chem. 47 (2008) 2552.
[12] R.B. Walsh, C.W. Padgett, P. Metrangolo, G. Resnati, T.W. Hanks, W.T. Pennington, Cryst. Growth Des. 1 (2001) 165.
[13] (a) J.A. Rodriguez-Velamazán, M. Castro, E. Palacios, R. Burriel, T. Kitazawa, T. Kawasaki, J. Phys. Chem. B 111 (2007) 1256;
(b) T. Kosone, C. Kachi-Terajima, T. Saito, T. Kitazawa, Chem. Lett. 37 (2008) 754.
[14] (a) T. Kosone, C. Kachi-Terajima, C. Kanadani, T. Saito, T. Kitazawa, Chem. Lett. 37 (2008) 422;
(b) T. Kosone, C. Kanadani, T. Saito, T. Kitazawa, Polyhedron 28 (2009) 1930.
[15] (a) A. Galet, V. Niel, M.C. Muñoz, J.A. Real, J. Am. Chem. Soc. 125 (2003) 14224;
(b) A. Galet, M.C. Muñoz, V. Martínez, J.A. Real, Chem. Commun. (2004) 2268.
[16] A. Galet, M.C. Muñoz, J.A. Real, Chem. Commun. (2006) 4321.
[17] A. Galet, A.B. Gaspar, G. Agustí, M.C. Muñoz, J.A. Real, Chem. Phys. Lett. 434 (2007) 68.
[18] J.A. Rodriguez-Velamazán, C. Carbonera, M. Castro, E. Palacios, T. Kitazawa, J.F. Létard, R. Burriel, Chem. Eur. J. 16 (2010) 8785.
[19] T. Kosone, I. Tomori, C. Kanadani, T. Saito, T. Michida, T. Kitazawa, Dalton Trans. 39 (2010) 1719.
[20] T. Kosone, Y. Suziki, S. Ono, C. Kanadani, T. Saito, T. Kitazawa, Dalton Trans. 39 (2010) 1786.
[21] (a) M. Serediuk, A.B. Gaspar, M. Verdaguer, F. Villain, P. Gütlich, Inorg. Chem. 48 (2009) 6130;
(b) M. Serediuk, A.B. Gaspar, V. Ksenofontov, Y. Galyametdinov, M. Verdaguer, F. Villain, P. Gütlich, Inorg. Chem. 49 (2010) 10022.
[22] G. Agustí, A.B. Gaspar, M.C. Muñoz, P.G. Lacroix, J.A. Real, Aust. J. Chem. 62 (2009) 1155.
[23] V. Niel, A.L. Thompson, A.E. Goeta, C. Enachescu, A. Hauser, A. Galet, M.C. Muñoz, J.A. Real, Chem. Eur. J. 11 (2005) 2047.
[24] A. Galet, M.C. Muñoz, A.B. Gaspar, J.A. Real, Inorg. Chem. 44 (2005) 8749.
[25] V. Niel, A.L. Thompson, M.C. Muñoz, A. Galet, A.E. Goeta, J.A. Real, Angew. Chem. Int. Ed. 42 (2003) 3760.
[26] G. Agustí, A.B. Gaspar, M.C. Muñoz, J.A. Real, Inorg. Chem. 46 (2007) 9646.
[27] A. Galet, A.B. Gaspar, M.C. Muñoz, G.V. Bukin, G. Levchenko, J.A. Real, Adv. Mater. 17 (2005) 2949.
[28] A. Galet, Ph.D. Thesis, University of Valencia, Spain, 2006.
[29] V. Niel, M.C. Muñoz, A.B. Gaspar, A. Galet, G. Levchenko, J.A. Real, Chem. Eur. J. 8 (2002) 2446.
[30] (a) K.A. Hofmann, F.A. Küspert, Z. Anorg, Allg. Chem. 15 (1897) 204;
(b) H.M. Power, J.H. Rainer, Nature 163 (1949) 566;
(c) H.M. Power, J.H. Rainer, J. Chem. Soc. (1952) 319;
(d) S. Nishikiori, H. Yoshikawa, Y. Sano, T. Iwamoto, Acc. Chem. Res. 38 (2005) 227.
[31] (a) T. Kitazawa, Y. Gomi, M. Takahashi, M. Takeda, M. Enomoto, A. Miyazaki, T. Enoki, J. Mater. Chem. 6 (1996) 119;
(b) G. Molnar, T. Kitazawa, L. Dubrovinsky, J.J. McGarvey, A. Bousseksou, J. Phys.: Condens. Matter 16 (2004) 1129;

(c) K. Hosoya, T. Kitazawa, M. Takahashi, M. Takeda, J.F. Meunier, G. Molnár, A. Bousseksou, J. Phys. Chem. Chem. Phys. 5 (2003) 1682.
[32] T. Kitazawa, M. Eguchi, M. Takeda, Mol. Cryst. Liq. Cryst. 341 (2000) 527.
[33] (a) V. Martínez, A.B. Gaspar, M.C. Muñoz, G.V. Bukin, G. Levchenko, J.A. Real, Chem. Eur. J. 15 (2009) 1096;
(b) T. Kitazawa, M. Takahashi, M. Enomoto, A. Miyazaki, T. Enoki, M. Takeda, J. Radioanal. Nucl. Chem. 239 (1999) 285.
[34] K. Nakao, S. Hayami, M. Akita, K. Inoue, Chem. Lett. 37 (2008) 292.
[35] V. Martínez, A.B. Gaspar, M.C. Muñoz, R. Ballesteros, N. Ortega-Villar, V.M. Ugalde-Saldívar, R. Moreno-Esparza, J.A. Real, Eur. J. Inorg. Chem. (2009) 303.
[36] V. Niel, J.M. Martínez-Agudo, M.C. Muñoz, A.B. Gaspar, J.A. Real, Inorg. Chem. 40 (2001) 3838.
[37] G. Molnár, V. Niel, J.A. Real, L. Dubrovinsky, A. Bousseksou, J.J. McGarvey, J. Phys. Chem. B 107 (2003) 3149.
[38] G. Molnár, T. Guillon, N.O. Moussa, L. Rechignat, T. Kitazawa, M. Nardone, A. Bousseksou, Chem. Phys. Lett. 423 (2006) 152.
[39] G. Agustí, S. Cobo, A.B. Gaspar, G. Molnár, N.O. Moussa, P.Á. Szilágyi, Villö Pálfi, C. Vieu, M.C. Muñoz, J.A. Real, A. Bousseksou, Chem. Mater. 20 (2008) 6721.
[40] T. Tayagaki, A. Galet, G. Molnár, M.C. Muñoz, A. Zwick, K. Tanaka, J.A. Real, A. Bousseksou, J. Phys. Chem. B 109 (2005) 14859.
[41] (a) S. Bonhommeau, G. Molnár, A. Galet, A. Zwick, J.A. Real, J.J. McGarvey, A. Bousseksou, Angew. Chem. Int. Ed. 44 (2005) 4069;
(b) S. Cobo, D. Ostrovskii, S. Bonhommeau, L. Vendier, G. Molnár, L. Salmon, K. Tanaka, A. Bousseksou, J. Am. Chem. Soc. 130 (2008) 9019.
[42] G. Agustí, Ph.D. Thesis, University of Valencia, Spain, 2009.
[43] (a) K.R. Dunbar, R.A. Heintz, Prog. Inorg. Chem. 45 (1997) 283;
(b) S. Ohkoshi, K.J. Hashimoto, Photochem. Photobiol. C 2 (2001) 71;
(c) O. Sato, Acc. Chem. Res. 36 (2003) 692;
(d) M. Verdaguer, G.S. Girolami, in: V. Miller, J.S.M. Drillon (Eds.), Magnetism: Molecules to Materials, Wiley-VCH, Weinheim, 2005, p. 283.
[44] W. Kosaka, K. Nomura, K. Hashimoto, S. Ohkoshi, J. Am. Chem. Soc. 127 (2005) 8590.
[45] D. Papanikolaou, S. Margadonna, W. Kosaka, S. Ohkoshi, M. Brunelli, K. Prassides, J. Am. Chem. Soc. 128 (2006) 8358.
[46] M. Arai, W. Kosaka, T. Matsuda, S. Ohkoshi, Angew. Chem. 120 (2008) 6991.
[47] M. Ohba, K. Yoneda, G. Agustí, M.C. Muñoz, A.B. Gaspar, J.A. Real, M. Yamasaki, H. Ando, Y. Nakao, S. Sakaki, S. Kitagawa, Angew. Chem. Int. Ed. 48 (2009) 4767.
[48] P.D. Southon, L. Liu, E.A. Fellows, D.J. Price, G.J. Halder, K.W. Chapman, B. Moubaraki, K.S. Murray, J.F. Létard, C.J. Kepert, J. Am. Chem. Soc. 131 (2009) 10998.
[49] G. Agustí, R. Ohtani, K. Yoneda, A.B. Gaspar, M. Ohba, J.F. Sánchez-Royo, M.C. Muñoz, S. Kitagawa, J.A. Real, Angew. Chem. Int. Ed. 48 (2009) 8944.
[50] C.M. Bell, M.F. Arendt, L. Gomez, R.H. Schmell, T.E. Mallouk, J. Am. Chem. Soc. 116 (1994) 8374.
[51] S. Cobo, G. Molnár, J.A. Real, A. Bousseksou, Angew. Chem. Int. Ed. 45 (2006) 5786.
[52] G. Molnár, S. Cobo, J.A. Real, F. Carcenac, E. Daran, C. Vieu, A. Bousseksou, Adv. Mater. 19 (2007) 2163.
[53] (a) I. Boldog, A.B. Gaspar, V. Martínez, P. Pardo-Ibañez, V. Ksenofontov, A. Bhattacharjee, P. Gütlich, J.A. Real, Angew. Chem. Int. Ed. 47 (2008) 6433;
(b) F. Volatron, L. Catala, E. Rivière, A. Gloter, O. Stephan, T. Mallah, Inorg. Chem. 47 (2008) 6584.
[54] V. Martínez, I. Boldog, A.B. Gaspar, V. Ksenofontov, A. Bhattacharjee, P. Gütlich, J.A. Real, Chem. Mater. 22 (2010) 4271.
[55] (a) A.P. Alivisatos, J. Phys. Chem. 100 (1996) 13226;
(b) M.D. Baker, A.D. Baker, J. Chem. Educ. 87 (2010) 280;
(c) G.A. Breaux, R.C. Benirschke, M.F. Jarrold, J. Chem. Phys. 121 (2004) 6502.
[56] J. Larionova, L. Salmon, Y. Guari, A. Tokarev, K. Molvinger, G. Molnár, A. Bousseksou, Angew. Chem. Int. Ed. 47 (2008) 8236.